



Bergische Universität Wuppertal

Fakultät für Mathematik und Naturwissenschaften

Institute of Mathematical Modelling, Analysis and Computational
Mathematics (IMACM)

Preprint BUW-IMACM 25/12







Sergey Pereselkov, Venedikt Kuz'kin, Matthias Ehrhardt, Sergey Tkachenko,
Alexey Pereselkov and Nikolay Ladykin

Effect of Irregular Bathymetry on Hologram Formation of a Moving Source in Shallow Water

August 18, 2025

<http://www.imacm.uni-wuppertal.de>

Effect of Irregular Bathymetry on Hologram Formation of a Moving Source in Shallow Water

Sergey Pereselkov ^{1,*}, Venedikt Kuz'kin ², Matthias Ehrhardt ³, Sergey Tkachenko ¹,
Alexey Pereselkov ¹ and Nikolay Ladykin ¹

¹ Mathematical Physics and Information Technology Department, Voronezh State University, 394018 Voronezh, Russia; pereselkov@yandex.ru (S.P.); tkachenko.edu@yandex.ru (S.T.); pereselkov.edu@yandex.ru (A.P.); ladykin.edu@yandex.ru (N.L.)

² Prokhorov General Physics Institute of the Russian Academy of Sciences, 119991 Moscow, Russia; kumiov@yandex.ru

³ Chair of Applied and Computational Mathematics, University of Wuppertal, Gaußstraße 20, 42119 Wuppertal, Germany; ehrhardt@uni-wuppertal.de

* Correspondence: pereselkov@yandex.ru

Abstract: This paper examines the effect of irregular bathymetry on the holographic reconstruction of the sound field generated by a moving source in shallow water. In this scenario, acoustic waves propagate along the path between the source and receiver. Spatial inhomogeneities in the waveguide, resulting from complex bottom topography, cause notable horizontal refraction of acoustic modes. The study focuses on how this horizontal refraction affects the structure of the interferogram and the hologram corresponding to the moving source. This investigation is carried out through numerical simulations that incorporate ray refraction due to irregularities in the waveguide. The interferogram, representing the received sound intensity in the frequency-time domain, and the hologram, obtained via a two-dimensional Fourier transform of the interferogram, are analyzed in the presence of spatial variability caused by non-uniform bathymetry. A key finding is that despite these irregularities, the hologram retains sufficient structural information to extract and reconstruct source parameters (e.g., range, velocity). The paper also provides a quantitative estimate of the reconstruction error associated with this approach.

Keywords: shallow water; irregular bathymetry; interferogram; hologram; horizontal refraction, moving source, source parameters estimation

1. Introduction

In recent years, *interferometric signal processing* (ISP) has attracted increasing scientific attention within the field of underwater acoustics. ISP exploits stable features of interference patterns generated by broadband acoustic fields in shallow water waveguides [1,2]. Comprehensive discussions of the theoretical foundations and methodological aspects of ISP can be found in seminal works [3–5]. Numerous studies have demonstrated the practical applications of ISP. For instance, in [6,7], ISP algorithms are used to determine waveguide-invariant parameters. The approach in [8] illustrates the use of ISP for processing weak signals, achieving performance improvements via array beamforming techniques. In [9], ISP is applied to classify seabed types using acoustic emissions from passing ships. The authors of [10] introduce a method for estimating the range to a source in shallow water conditions based on ISP analysis. A range-independent invariant estimation framework utilizing ISP principles is described in [11]. Additionally, the work in [12] interprets interference fringe structures in terms of eigenray or eigenbeam arrival times. Finally, adaptations of ISP for deep-water passive sonar applications are reported in [13,14], highlighting the method's flexibility for diverse underwater acoustic scenarios.

Among the various techniques in interferometric signal processing (ISP), *holographic signal processing* (HSP) is a particularly promising direction, as discussed in [15–17]. The essential physical

concepts and mathematical framework for creating holograms were first formulated in [15]. In the HSP methodology, a quasi-coherent summation of sound intensity in the joint frequency-time domain yields an *interferogram* $I(\omega, t)$, cf. [16,17]. To investigate the spatial distribution of the accumulated intensity, a two-dimensional Fourier transform (2D-FT) is then performed on $I(\omega, t)$. The outcome of this transformation, known as the *Fourier hologram* (or simply the *hologram*), is expressed as $F(\tau, \tilde{\nu}) = \mathcal{F}_{2D}\{I(\omega, t)\}$. Here, $F(\tau, \tilde{\nu})$ represents a redistribution of the acoustic energy from $I(\omega, t)$ into distinct, localized focal regions that emerge as a consequence of modal interference patterns. In essence, a hologram is a variant of sound field focusing [18], which is implemented in the Fourier- Space using a single receiver.

In the early stages of developing the HSP method [15–17] and its verification [19], it was generally assumed that the properties of the acoustic waveguide remained unchanged in space and time. However, in reality, acoustic signals often propagate through waveguides with significant inhomogeneities. In shallow water environments, this variability often results from hydrodynamic disturbances generated by internal waves. The first experimental study of HSP applied to a stationary source under realistic environmental conditions was reported in [20,21]. The study showed that hydrodynamic perturbations distort the interferogram $I(\omega, t)$ and expand the focal regions observed in the reconstructed hologram $F(\tau, \tilde{\nu})$. When inhomogeneities are present, the hologram can be presented as the sum of two components: One is produced by the unperturbed waveguide, and the other is associated with the perturbations.

This decomposition was used in [20,21] to interpret the measurements obtained during the SWARM’95 experiment [22,23]. During SWARM’95, the dominant source of waveguide variability was *intense internal waves* (IWs) [23–26], a common hydrodynamic phenomenon in the ocean [24–26]. The experiment utilized two distinct acoustic propagation paths, both of which were generated by the same source and received by two vertically oriented arrays located in different positions. The first path was aligned at a small angle to the IW wavefront; in this geometry, IWs produce strong horizontal refraction of acoustic rays. The second path was perpendicular to the IW wavefront so that the internal waves traveled along the propagation path from the source to the receiver. Under these conditions, horizontal refraction was absent, but substantial redistribution of acoustic energy occurred between modes, i.e., mode coupling. The effects of IWs have been discussed in our prior works [27–29].

In addition to internal waves, an important factor contributing to the spatial inhomogeneity of a shallow water waveguide is the bottom relief, or irregularities in the bathymetry. The properties of these irregularities vary depending on the region being studied. Nevertheless, general patterns characteristic of many shallow-water areas across the world ocean exist. Experimental observations [30–37] indicate that the seabed on the continental shelf is generally smooth, with deviations from the average depth not exceeding tens of meters vertically. At the same time, the range of bottom relief variations is extensive [32–35], with horizontal scales spanning from a few centimeters to hundreds of kilometers. This structure of bathymetric irregularities, similar to internal waves, leads to significant acoustic effects associated with horizontal refraction and mode coupling. Therefore, the effect of irregular bathymetry on hologram formation from a moving source in shallow water is an important factor in the robustness of the HSP method that should be researched.

The aim of this paper is to study the effect of irregular bathymetry on holographic sound field reconstruction generated by a moving source in a shallow water environment. Spatial inhomogeneities introduced by complex bottom topography along the acoustic propagation path between the source and receiver cause pronounced horizontal refraction of acoustic modes. This refraction alters the spatial-temporal structure of the received field, which can degrade the performance of holographic processing techniques. We conduct our analysis through high-fidelity numerical simulations that explicitly model the refraction of acoustic modes induced by the non-uniform bathymetric features of the waveguide. Within this framework, we examine the interferogram, which is defined as the distribution of received sound intensity in the joint frequency-time domain, and its corresponding hologram. The hologram is obtained via the two-dimensional Fourier transform of the interferogram.

The study focuses on how spatial variability from the irregular seabed modifies the fine- and large-scale features of these representations. A key finding is that despite the significant distortions introduced by horizontal refraction, the hologram retains a coherent and interpretable structure containing sufficient information for the reliable extraction and reconstruction of key source parameters, including range and velocity. This finding demonstrates that the holographic method is resilient to the effects of complex bathymetry and remains a viable approach for characterizing sources in realistic shallow water conditions. The paper also provides a quantitative evaluation of reconstruction error, offering practical insights into accuracy limits under varying degrees of bottom irregularity.

The paper consists of five sections. Section 1, the introduction, describes the current state of the problem under consideration. Section 2 presents a three-dimensional model of a shallow water waveguide in the presence of bottom irregularities. Three cases of spatial dependence of $H(\mathbf{r})$ are considered. These cases are: a waveguide with regular bathymetry (Section 2.1); a littoral wedge waveguide (Section 2.2); and a canyon waveguide (Section 2.3). Section 3 describes the mathematical models of the interferogram $I(\omega, t)$ and the hologram $F(\tau, \tilde{v})$ of a moving source in a shallow water waveguide with an irregular bottom. Section 3 is organized into six distinct subsections, each addressing a specific aspect of the sound field in a shallow water waveguide with irregular bathymetry. Subsection 3.1 introduces the theoretical framework for modeling the sound field in such a waveguide, employing the combined approach of vertical modes and horizontal ray approximations. This subsection outlines how these two methods interact to describe three-dimensional sound propagation in a complex underwater environment. Subsection 3.2 develops the Sturm-Liouville eigenvalue and eigenfunction problem, incorporating boundary conditions that model a free surface at the top and a solid or lossy bottom at the base of the waveguide. The solution to this problem yields a set of vertical modes that form the basis for subsequent acoustic field calculations. Subsection 3.3 shifts the focus to the mode ray description in the horizontal plane. Here, we derive the eikonal equation (which governs phase evolution) and the transport equation (which describes amplitude variation) for mode rays traveling through a waveguide whose bottom topography varies spatially. These equations form the foundation for predicting how sound energy is refracted, focused, or dispersed by bathymetric irregularities. Subsection 3.4 addresses an alternative, yet complementary, representation: the parabolic mode equations in the horizontal plane. This formulation efficiently simulates horizontal sound propagation over large distances, especially in environments where the slope and curvature of the bathymetry are significant. Subsection 3.5 presents the methodology for constructing a sound field interferogram in a waveguide with irregular bathymetry. The interferogram is a visualization tool that reveals patterns of constructive and destructive interference between modes, offering insight into the spatial structure of the acoustic field. Finally, Subsection 3.6 examines the formation and analysis of the sound field hologram for the same complex waveguide environment. This technique enables the reconstruction of the three-dimensional structure of the acoustic field, offering a deeper understanding of how bathymetric features impact wave propagation.

Section 4 considers the numerical modeling results for different cases of waveguide bathymetry. This section is divided into six subsections, each of which focuses on a particular scenario of acoustic wave propagation involving stationary or moving sound sources in various waveguide environments. Subsection 4.1 examines the sound field generated by a stationary source in a waveguide with regular bathymetry, where the seabed topography is uniform and does not vary significantly with horizontal position. This subsection outlines the theoretical formulation and provides representative results illustrating how sound propagates in this idealized environment. Subsection 4.2 extends the analysis to the sound field of a moving source in the same regular-bathymetry waveguide. Here, the influence of source motion on the spatial and temporal characteristics of the acoustic field is examined, including effects such as frequency shifts, beam pattern distortion, and the evolution of the interference structure. Subsection 4.3 turns to a littoral wedge waveguide configuration and investigates the sound field produced by a stationary source. In this environment, the seabed rises toward the shoreline, creating a wedge-shaped bathymetry that introduces complex modal coupling, refraction, and energy redistri-

bution effects. Subsection 4.4 considers the case of a moving source in a littoral wedge waveguide, emphasizing how the combination of source motion and sloping bathymetry modifies acoustic propagation. It places special focus on changes in mode excitation, shifting interference fringes, and potential shadow zones that may form due to the wedge geometry. Subsection 4.5 explores the sound field of a stationary source in a canyon-shaped waveguide where the seabed features a deep, narrow depression. The analysis examines how such a topographic feature traps, channels, or scatters sound energy, resulting in different spatial field patterns than those of regular bathymetry. Finally, Subsection 4.6 investigates the sound field generated by a moving source in a canyon waveguide. This scenario combines the effects of the source's motion with the canyon's strong topographic influence, revealing unique propagation behaviors, such as enhanced mode conversion, directional energy focusing, and localized acoustic hotspots. The main findings of the paper are summarized in Section 5.

2. Waveguide Model with Irregular Bathymetry

In this section, we present the three-dimensional model of the shallow water waveguide with irregular bathymetry that was used in our study (see Figure 1).

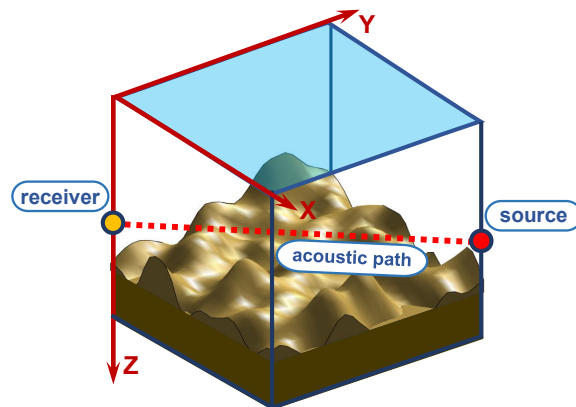


Figure 1. Model of a shallow water waveguide with irregular bathymetry.

The shallow water waveguide is defined in a Cartesian coordinate system (x, y, z) where the x and y axes lie in the horizontal plane and the z -axis points downward from the free surface at $z = 0$. The waveguide is modeled as a water layer with spatially and temporally varying sound speed $c(\mathbf{r}, z)$ and density $\rho(\mathbf{r}, z)$. Here, $\mathbf{r} = (x, y)$ denotes the horizontal position vector. The water column is bounded above by the free surface at $z = 0$ and below by the sea bottom at $z = z_b(\mathbf{r})$.

The seabed's density and refractive index are given by ρ_b and $n_b(1 + i\kappa)$, respectively [38,39], where κ is the attenuation factor, defined as $\kappa = \chi c_b / (54.6f)$. In this expression, χ represents the bottom loss coefficient. c_b is the acoustic velocity in the bottom layer, and f is the sound frequency.

The spatial variation of the bathymetry can be expressed as follows:

$$z_b(\mathbf{r}) = H(\mathbf{r}) + \tilde{H}(\mathbf{r}), \quad (1)$$

where $H(\mathbf{r})$ describes *general relief*, and $\tilde{H}(\mathbf{r})$ accounts for *meso- and microrelief* of irregular bathymetry. The characteristics of bottom irregularities depend on the specific study area. However, some general features are typical of many shallow water regions of the world's oceans. According to the results of experimental studies [30–37], the seabed surface on the continental shelf is relatively smooth, with deviations from the mean seabed level not exceeding several tens of meters.

At the same time, the spectrum of bottom irregularities is very broad [33–37] – the linear dimensions range from centimeters to hundreds of kilometers. The entire spectrum can be divided into three parts: *general relief*, *mesorelief*, and *microrelief*. The *general relief*, which characterizes the main geomorphological features (ridges, plains, depressions, etc.) has dimensions of approximately 10^4 to 10^5 meters. The *mesorelief* includes relief features stretching approximately 10^2 to 10^3 meters. The

microrelief (formed by ripples, stones, hummocks, etc.) has spatial scales of approximately 10^{-2} to 10^1 meters. According to this classification, the first large-scale component of the seabed relief corresponds to regular changes in waveguide parameters depending on the frequency. The other two components, mesorelief and microrelief, correspond to random changes.

In our paper, we will analyze the influence of the source hologram structure on the spatial variation of the bathymetry associated with the *general relief* $H(\mathbf{r})$. We will assume that the *mesorelief* and the *microrelief* are absent: $\tilde{H}(\mathbf{r}) = 0$. Thus, we will suppose that:

$$z_b(\mathbf{r}) = H(\mathbf{r}) = H(x, y), \quad (2)$$

Let us perform a comparative analysis of the spatial dependence of $H(\mathbf{r})$ in three cases (see Figure 2). The cases are a waveguide with regular bathymetry (Figure 2(a)), a littoral wedge waveguide (Figure 2(b)), and a canyon waveguide (Figure 2(c)).

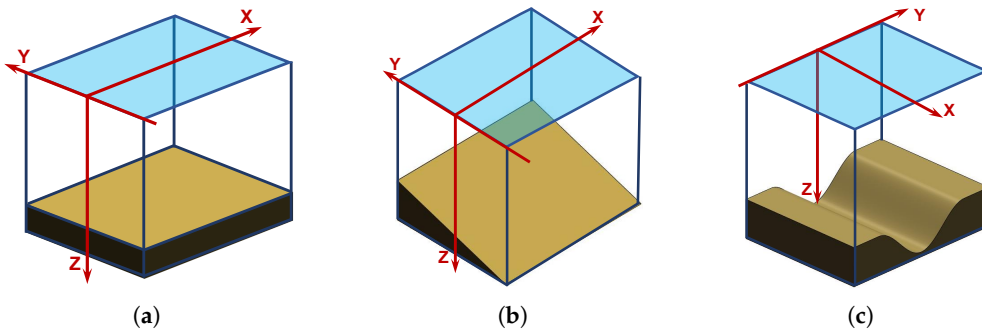


Figure 2. Models of shallow water waveguides: (a) regular waveguide; (b) littoral wedge waveguide; (c) canyon waveguide.

2.1. The Regular Waveguide

Consider the regular waveguide model (Figure 2(a)). In this model, the waveguide is shallow and uniform in depth across its entire horizontal extent, with no variation in the seabed elevation. This highly idealized representation is a standard benchmark in underwater acoustics because it provides a controlled environment in which the influence of environmental parameters, such as spatial variations in the sound speed profile of the water column, can be examined independently of changes in seabed topography. By eliminating bottom relief as a factor, one can focus on fundamental propagation mechanisms, validate analytical models, and compare numerical methods under consistent conditions.

According to the general model (Figure 2(a)) of a shallow water waveguide, we use the Cartesian coordinate system (x, y, z) , where the x and y axes lie in the horizontal plane, and the z -axis points downward from the free surface at $z = 0$. The seabed is described by the depth function $z_b(\mathbf{r}) = H(\mathbf{r}) = H(x, y)$. In the case of a regular waveguide model, the depth is assumed to be constant in both the x and y directions:

$$H(\mathbf{r}) = H(x, y) = H_0. \quad (3)$$

Regular waveguide parameters:

- H_0 is the reference depth of the waveguide (in meters).

This configuration creates a waveguide through which acoustic modes can propagate without experiencing horizontal refraction or mode coupling due to bottom relief. The uniform bathymetry ensures translational isotropy in all horizontal directions.

2.2. The Littoral Wedge Waveguide

Consider the littoral wedge waveguide (see Figure 2(b)). The littoral wedge model describes a waveguide in shallow water in which the water depth changes linearly in one horizontal direction. This simplified yet representative configuration is a useful approximation of real-world nearshore

environments, including continental shelves, gently sloping seabeds, tidal flats, and coastal approaches. In these settings, the seafloor gradually inclines, either descending toward deeper offshore waters or rising toward the shoreline. The model provides a convenient framework for investigating sound propagation in coastal zones, where depth variations strongly influence acoustic properties, alter underwater wave paths and speeds, and affect their interaction with the seabed and free surface. The littoral wedge model captures the essential geometric features of sloping-bottom environments, enabling researchers to analyze complex shallow-water acoustics in a more tractable and controlled manner.

We use the same Cartesian coordinate system (x, y, z) (Figure 2(b)), where the x and y axes lie in the horizontal plane and the z -axis points downward from the free surface at $z = 0$. The seabed is described by the depth function $z_b(\mathbf{r}) = H(\mathbf{r}) = H(x, y)$. In this case, the littoral wedge is assumed to vary only in the y -direction:

$$H(\mathbf{r}) = H(x, y) = H(y) = H_0 - k_0 y. \quad (4)$$

Littoral wedge waveguide parameters:

- H_0 is the reference depth of the waveguide at $x = 0$ (in meters);
- k_0 is the slope coefficient (meters in the vertical direction per meter in the horizontal direction). For $k_0 > 0$, the depth decreases as y increases; for $k_0 < 0$, the depth increases as y increases; for $k_0 = 0$, the depth remains constant as y changes;
- α is the slope angle of the seabed plane ($k_0 = \tan \alpha$) relative to the horizontal plane (radians).

In the case of a littoral wedge waveguide, the geometry supports the development of a guided acoustic environment. In this environment, modal propagation is subject to either pronounced horizontal refraction or mode coupling arising from bottom relief. The gradual seabed slope characteristic of the wedge profile induces horizontal refraction of acoustic modes when they propagate at small angles relative to the x -axis. Conversely, when propagation occurs at small angles relative to the y -axis, mode coupling within the acoustic field becomes the dominant effect. These bathymetric irregularities give rise to substantial anisotropy in the acoustic propagation environment with distinct directional dependencies in sound energy transport.

2.3. The Canyon Waveguide

Consider the canyon waveguide model (see Figure 2(c)). This model describes a shallow water acoustic environment featuring a pronounced, localized seabed depression, such as a trench or submarine canyon. This distinctive yet representative configuration is a useful approximation of the bathymetric conditions commonly found in the real world along continental margins, fjord entrances, and near underwater escarpments. In these settings, the seafloor includes steeply sloping sidewalls and a narrow, elongated axis that together create a confined acoustic channel.

These features can significantly impact the propagation of underwater sound by modifying the modal structure, trapping acoustic energy within the canyon boundaries, guiding sound waves along the canyon axis, and focusing beams through refractive effects. The model provides a practical framework for studying acoustic processes in complex coastal and shelf-edge environments where abrupt depth changes greatly impact wave speeds, transmission loss, and mode coupling. By capturing the essential geometric characteristics of submarine canyons, the canyon waveguide model allows researchers to study the interaction between topography and sound in a more manageable and controlled environment.

As before, we consider a Cartesian coordinate system (x, y, z) (Figure 2(c)), where the x and y axes define the horizontal plane and the z -axis points downward from the free surface at $z = 0$. The seabed profile is represented by the depth function $z_b(\mathbf{r}) = H(\mathbf{r}) = H(x, y)$. For the canyon waveguide model,

the bathymetry includes a localized depression in the y -direction. The canyon axis is oriented along the x -direction. The mathematical model of the canyon waveguide bathymetry has the following form:

$$H(\mathbf{r}) = H(x, y) = H_0 + A_0 \text{sech}^2(y/L_0), \quad (5)$$

Canyon waveguide parameters:

- H_0 is the reference depth of waveguide (in meters);
- A_0 is the canyon depth (in meters);
- L_0 is the canyon's half-width (in meters).

In the case of a canyon waveguide, the seabed features a pronounced depression with steep sidewalls that form a natural acoustic channel. This configuration creates a complex shallow-water acoustic environment in which modal propagation is influenced by horizontal refraction and inter-modal coupling driven by abrupt bathymetric variations. When acoustic waves propagate along the canyon's axis — typically oriented in the x -direction, the steep lateral gradients in depth can refract energy toward the canyon's centerline, effectively trapping and guiding it over long distances. Conversely, when propagation is oriented across the canyon (i.e., in the y -direction), the strong transverse bathymetric variation promotes significant mode coupling and energy redistribution between modes. This highly non-uniform bathymetry induces pronounced anisotropy in acoustic propagation characteristics, resulting in direction-dependent transmission loss, altered modal dispersion properties, and the spatial focusing or defocusing of acoustic beams. Capturing these effects, the canyon waveguide model provides a powerful framework for investigating the interplay between complex topography and underwater sound in continental shelf environments.

A summary of the three cases of the shallow water waveguide models – *regular waveguide*, *littoral wedge*, and *canyon* – is presented in Table 1.

Table 1. Models of shallow water waveguides

Model	Depth Function $H(\mathbf{r})$	Model Parameters
1. Regular Waveguide	$H(\mathbf{r}) = H_0$	H_0 – reference depth
2. Littoral Wedge	$H(\mathbf{r}) = H_0 - k_0 y$	H_0 – reference depth, k – slope coefficient.
3. Canyon	$H(\mathbf{r}) = H_0 + A_0 \text{sech}^2(y/L_0)$	H_0 – reference depth, A_0 – canyon depth, L_0 – canyon's half-width.

3. Interferogram and Hologram in the Presence of Irregular Bathymetry

This section presents a model of the source interferogram and hologram within a shallow-water waveguide featuring irregular bathymetry. It is divided into six parts. Subsection 3.1 describes the sound field model in a waveguide with irregular bathymetry using the framework of vertical modes and the approximation of horizontal rays. Subsection 3.2 formulates the Sturm-Liouville eigenvalue and eigenfunction problem with boundary conditions representing a free surface and a bottom in a shallow-water waveguide. This problem is used to determine the vertical modes. Subsection 3.3 derives the eikonal and transport equations for mode rays in the horizontal plane for a waveguide with irregular bathymetry. Subsection 3.4 considers the mode parabolic equations in the horizontal plane for the same waveguide environment. Subsection 3.5 presents the sound field interferogram in a waveguide with irregular bathymetry. Finally, Subsection 3.6 analyzes the sound field hologram in a waveguide with irregular bathymetry.

Our work is based on computational modeling of acoustic wave propagation in three-dimensional (3D) shallow-water waveguides with spatially varying properties. Variations in the medium, particularly those caused by irregularities in the seabed topography, can substantially modify the sound field through mechanisms such as refraction and scattering. Accurate broadband simulations at low frequencies in such complex 3D settings require considerable computational resources, often making it necessary to apply advanced numerical algorithms together with high-performance computing systems to achieve physically realistic predictions. There are five main categories of numerical techniques for modeling sound propagation in inhomogeneous shallow-water environments [40]: (1) Three-Dimensional Helmholtz Equation (3DHE) Methods [41–43]; (2) Three-Dimensional Parabolic Equation (3DPE) Methods [44–50]; (3) Three-Dimensional Ray-Based (3DR) Methods [51,52]; (4) Vertical Mode Combined with Two-Dimensional Modal Parabolic Equation (VMMPE) Methods [53–55]; (5) Vertical Mode Combined with Horizontal Ray (VMHR) Methods [56,57].

In the present study, we examine low-frequency acoustic fields within two narrow frequency bands (100–140 Hz) in a shallow-water environment. Spatial inhomogeneities in this environment are attributed to bathymetric irregularities aligned along the propagation path from the source to the receiver. These variations in the seabed cause pronounced horizontal refraction effects. Of the five categories of numerical approaches described, the VMHR and VMMPE frameworks are the most appropriate for our problem. These methods are well-suited for simulating the propagation of low-frequency waves in shallow water settings affected by seabed topography because they rigorously account for boundary conditions and effectively capture the physical processes associated with horizontal refraction.

In contrast, 3DR models are optimized for high-frequency applications and cannot adequately resolve modal behavior in shallow-water, low-frequency conditions. While 3DHE and 3DPE models can yield highly accurate solutions, they are too computationally expensive for the fully three-dimensional problem considered here. The VMHR and VMMPE approaches, on the other hand, strike an efficient balance between physical realism and numerical feasibility, enabling the accurate modeling of horizontal refraction phenomena. Consequently, these methods are adopted as the primary computational tools for simulating sound propagation under the influence of along-acoustic-path bathymetric irregularities in this work.

It should be noted that the influence of ocean waveguide bathymetric irregularities on acoustic field propagation has been investigated for several decades by numerous authors (see, e.g., [58–69]). However, in all of these studies, the primary focus has been on the characteristics of the acoustic field structure in shallow water waveguides with irregular bathymetry. The objective of the present work, by contrast, is to analyze the effect of bathymetric irregularities on the structure of the acoustic source hologram.

3.1. Sound Field

Within the framework of the VMHR and VMMPE approaches, the complex acoustic field in a shallow waveguide, influenced by bathymetric irregularities and described by equations (1)–(5), can be expressed as follows, cf. [38,39]:

$$p(\mathbf{r}, z, \omega) = \sum_{m=0}^M P_m(\mathbf{r}, \omega) \phi_m(z, \omega), \quad (6)$$

Here, $\mathbf{r} = (x, y)$ denotes the horizontal position vector of the source, P_m represents the amplitude of the m -th mode, and $\phi_m(z, \omega)$ denotes the vertical structure (mode shape) of the corresponding acoustic mode in a waveguide unaffected by bathymetric irregularities.

3.2. Vertical Modes

For each mode, the complex horizontal wavenumber is expressed as

$$\xi_m(\mathbf{r}, \omega) = h_m(\mathbf{r}, \omega) + i \gamma_m(\mathbf{r}, \omega), \quad (7)$$

where h_m and γ_m denote its real and imaginary components, respectively. The summation is carried out over M , the total number of propagating modes included in the model. Consequently, the acoustic pressure field p is a function of the angular frequency $\omega = 2\pi f$. The modal eigenfunctions $\phi_m(z, \omega)$ and their corresponding complex wavenumbers ξ_m are determined by solving a Sturm–Liouville boundary-value problem with a free-surface condition at the top and a bottom boundary condition at $z = H$, as described in [38,39]:

$$\frac{d^2 \phi_m(\omega, z)}{dz^2} + k^2 \bar{n}^2(z) \phi_m(\omega, z) = \xi_m^2 \phi_m(\omega, z), \quad (8)$$

$$\phi_m(\omega, 0) = 0, \quad \phi_m(\omega, H) + g(\xi_m) \left. \frac{d\phi_m(\omega, z)}{dz} \right|_{z=H} = 0, \quad (9)$$

with

$$g(\xi_m) = \frac{\eta}{\sqrt{\xi_m^2 - k^2 n_b^2 (1 + i \varkappa)}}. \quad (10)$$

The set of eigenfunctions $\phi_m(\omega, z)$ is normalized according to

$$\int_0^H \phi_l \phi_m dz + \eta \int_H^\infty \phi_l \phi_m dz = \delta_{ml}, \quad (11)$$

where δ_{ml} denotes the Kronecker delta.

3.3. Mode Rays in the Horizontal Plane

The dependence $P_m(\mathbf{r}, \omega)$ determines the distribution of the modal amplitude in the horizontal plane [56,57]:

$$\Delta_r P_m + h_m^2(\mathbf{r}, \omega) P_m = 0. \quad (12)$$

Within the ray approximation, $P_m(\mathbf{r}, \omega)$ can be represented as follows:

$$P_m(\mathbf{r}, \omega) = \sum_k A_{mk}(\mathbf{r}, \omega) e^{i\theta_{mk}(\mathbf{r}, \omega)}. \quad (13)$$

Here, $A_{mk}(\mathbf{r}, \omega)$ and $\theta_{mk}(\mathbf{r}, \omega)$ are determined by the eikonal and transport equations:

$$(\nabla_r \theta_{mk})^2 = h_m^2 n_m^2(\mathbf{r}, \omega), \quad 2 \nabla_r A_{mk} \nabla_r \theta_{mk} + A_{mk} \nabla_r^2 \theta_{mk} = 0, \quad (14)$$

where $n_m(\mathbf{r}, \omega) = h_m(\mathbf{r}, \omega)/h_m^0$. Here $h_m^0(\omega)$ is the horizontal wavenumber of the mode for the reference depth H_0 . As seen from Eq. (13), a significant drawback of the ray approach is the problem of accounting for multiple rays arriving at the observation point.

3.4. Mode Parabolic Equations in Horizontal Plane

The distribution of the modal amplitude $P_m(\mathbf{r}, t)$ is better suited for numerical calculations of the sound field, and is represented within the framework of the parabolic approximation as [44,45]:

$$P_m(\mathbf{r}, \omega) = F_m(\mathbf{r}, \omega) \exp(ih_m r), \quad (15)$$

where $F_m(\mathbf{r}, \omega)$, under the assumption $\partial F_m / \partial x \ll h_m F_m$, satisfies the equation:

$$\frac{\partial F_m}{\partial x} = \frac{i}{2h_m} \frac{\partial^2 F_m}{\partial y^2} + \frac{ih_m}{2} (n_m^2(\mathbf{r}, \omega) - 1) F_m. \quad (16)$$

The mode amplitude $P_m(\mathbf{r}, \omega, t)$ is determined as the solution of the parabolic equation:

$$\frac{\partial P_m}{\partial x} = \frac{i}{2\bar{h}_m} \frac{\partial^2 P_m}{\partial y^2} + \frac{i\bar{h}_m}{2} (n_m^2(\mathbf{r}, \omega, t) - 1) P_m, \quad (17)$$

where $n_m(\mathbf{r}, \omega)$ denotes the horizontal refractive index of the m -th acoustic mode in the waveguide in presence of the bathymetric irregularities:

$$n_m(\mathbf{r}, \omega, t) = h_m(\mathbf{r}, \omega, t) / h_m^0. \quad (18)$$

Here, $h_m^0(\omega)$ is the horizontal wavenumber of the mode for the reference depth H_0 . The numerical solution of Eq. (17) is performed using the "Split Step Fourier" (SSF) algorithm [44,45]:

$$P_m(x + \Delta x, y, \omega, t) = \exp[-i\bar{h}_m \Delta x U_m(x, y, \omega, t)] \times \mathcal{F}^{-1} \left\{ \exp[i\bar{h}_m \Delta x T_m(h)] \times \mathcal{F}[P_m^*(x, y, \omega, t)]^* \right\}. \quad (19)$$

Here \mathcal{F} is the Fast Fourier Transformation, \mathcal{F}^{-1} denotes the inverse Fast Fourier Transformation, $T_m(h) = 0.5(h/\bar{h}_m)^2$ is the operator in the Fourier Space of wavenumbers \bar{h}_m , $U_m(x, y, \omega, t) = -0.5(n_m^2(x, y, \omega, t) - 1)$ is the operator in the space of coordinates (x, y) in the horizontal plane. To specify the initial conditions in the calculations using the scheme Eq. (19), it was assumed that the source, located at the point with coordinates $(x_0, y = 0)$, emits a field in the Fourier space described by the expression:

$$A_m \exp \left\{ -\frac{h^2}{2\Delta_m^2} \right\}. \quad (20)$$

The parameter A_m defines the modal amplitude and depends on the mode value at the source depth. The parameter $\Delta_m = h_m \sin \varphi_{\max}$ characterizes the range of initial beam angles φ taken into account in the calculation. The angle φ is measured from the x -axis.

3.5. Interferogram

Within the VMHR and VMMPE framework, see Eq. (6), the interferogram $I(\omega, t)$ for a moving source in the frequency-time domain (ω, t) can be expressed as

$$\begin{aligned} I(\omega, t) &= \sum_m \sum_n A_m(\omega, t) A_n^*(\omega, t) \exp[i h_{mn}(\omega) (x_0 - vt)] \\ &= \sum_m \sum_n I_{mn}(\omega, t), \quad m \neq n, \end{aligned} \quad (21)$$

where $h_{mn}(\omega) = h_m(\omega) - h_n(\omega)$. The term $I_{mn}(\omega, t)$ represents the partial interferogram resulting from the interaction between the m -th and n -th modes. The quantity $A_m(\omega, t)$ denotes the amplitude of the m -th mode,

$$A_m(\omega, t) = P_m(\omega, t) \phi_m(z, \omega) \exp(-i h_m r), \quad (22)$$

With x_0 as the initial position of the source at $t_0 = 0$, t as the current time, and v as the source velocity, The superscript "*" indicates complex conjugation. The restriction $m \neq n$ ensures that the mean (auto-term) component is excluded from $I(\omega, t)$.

3.6. Hologram

In this part of the study, we analyze the holographic representation of an acoustic source in motion and take into account the effects of horizontal refraction due to bathymetric irregularities. A two-dimensional Fourier transform (2D-FT) is applied to the interferogram $I(\omega, t)$ given by Eq. (18) in joint frequency-time space (ω, t) to extract the holographic information. The result is the hologram $F(\tau, \tilde{\nu})$ in the form

$$\begin{aligned} F(\tau, \tilde{\nu}) &= \sum_m \sum_n \int_0^{\Delta t} \int_{\omega_1}^{\omega_2} I_{mn}(\omega, t) \exp[i(\tilde{\nu}t - \omega\tau)] dt d\omega \\ &= \sum_m \sum_n F_{mn}(\tau, \tilde{\nu}), \end{aligned} \quad (23)$$

where τ denotes the time delay, and $\tilde{\nu} = 2\pi\nu$ is the angular frequency variable in the hologram domain. The function $F_{mn}(\tau, \tilde{\nu})$ represents the contribution from the interference between modes m and n . Frequency integration is performed over the interval $\omega_1 = \omega_0 - \Delta\omega/2$ to $\omega_2 = \omega_0 + \Delta\omega/2$. Here, $\Delta\omega$ is the signal bandwidth, ω_0 is the reference (central) frequency, and Δt corresponds to the total observation time.

For subsequent derivations, a first-order (linear) approximation for the modal dispersion is employed:

$$h_m(\omega) \approx h_m(\omega_0) + \left. \frac{dh_m}{d\omega} \right|_{\omega=\omega_0} (\omega - \omega_0). \quad (24)$$

If the modal amplitudes P_m and the source spectrum vary slowly with frequency compared to the rapid oscillations of $\exp[ih_m(\omega)(x_0 + vt)]$, the partial hologram in Eq. (15) can be recast in the compact form

$$\begin{aligned} F_{mn}(\tau, \tilde{\nu}) &= A_m(\omega_0) A_n^*(\omega_0) \Delta\omega \Delta t \exp[i\Phi_{mn}(\tau, \tilde{\nu})] \times \\ &\quad \times \frac{\sin\left\{ \left[x_0 \frac{dh_{mn}(\omega_0)}{d\omega} - \tau \right] \frac{\Delta\omega}{2} \right\} \sin\left\{ [v h_{mn}(\omega_0) + \tilde{\nu}] \frac{\Delta t}{2} \right\}}{\left[x_0 \frac{dh_{mn}(\omega_0)}{d\omega} - \tau \right] \frac{\Delta\omega}{2} [v h_{mn}(\omega_0) + \tilde{\nu}] \frac{\Delta t}{2}}, \end{aligned} \quad (25)$$

where $\Phi_{mn}(\tau, \tilde{\nu})$ denotes the phase of the partial hologram $F_{mn}(\tau, \tilde{\nu})$:

$$\Phi_{mn}(\tau, \tilde{\nu}) = \left(\frac{\tilde{\nu} \Delta t}{2} - \tau \omega_0 \right) + h_{mn}(\omega_0) \left(\frac{\Delta t}{2} v + x_0 \right). \quad (26)$$

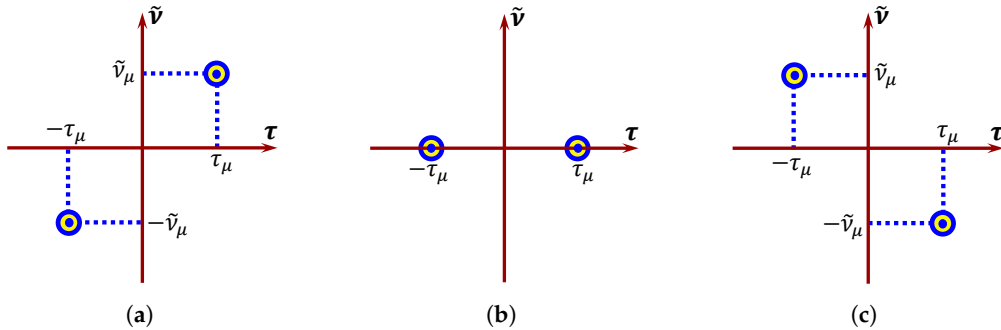


Figure 3. The structure of the partial hologram $F_{mn}(\tau, \tilde{\nu})$ for three different source motion scenarios: (a) the source approaches the receiver; (b) the source–receiver distance remains fixed; (c) the source recedes from the receiver.

As Eq. (25) shows, the hologram is concentrated in two regions of the $(\tilde{\nu}, \tau)$ plane that are symmetric with respect to the origin (see Fig. 3). This symmetry stems from the relation $F_{mn}(\tilde{\nu}, \tau) = F_{nm}(-\tilde{\nu}, -\tau)$. When the radial velocity is negative ($v < 0$), corresponding to a trajectory angle $\pi/2 < \varphi \leq \pi$, the hologram appears in quadrants I and III of the $(\tilde{\nu}, \tau)$ plane (Fig. 3a). When the

radial velocity is zero ($v = 0$), meaning the source-receiver distance remains unchanged, the hologram lies along the τ -axis (Fig. 3b). A positive radial velocity ($v > 0$), associated with a trajectory angle $0 \leq \varphi < \pi/2$, places the hologram in quadrants II and IV (Fig. 3c).

These spatial patterns allow us to determine from the hologram whether the source is approaching or receding from the receiver. For the focal spot, the expressions for radial velocity and initial source range are given by the following equations:

$$\dot{v} = -k_v \tilde{v}_\mu, \quad \dot{x}_0 = k_x \tau_\mu, \quad (27)$$

where

$$k_v = (m - n) \left(h_{mn}(\omega_0) \right)^{-1}, \quad k_x = (m - n) \left(dh_{mn}(\omega_0)/d\omega \right)^{-1}. \quad (28)$$

Consider the angular distribution of the spectral density of the hologram $F(\tau, \tilde{v})$:

$$G(\chi) = \int_0^{\Delta\tau} |F(\tau, \chi\tau)| d\tau \quad (29)$$

The function $G(\chi)$ has maximum value at $\chi = \chi_{\max}$ if the source is present. The direction of the maximum value is defined by ε . The maximum value of $G(\chi_{\max})$ is two or more times higher than the values in the other directions ($\chi \neq \chi_{\max}$):

$$G(\chi_{\max}) \geq 2G(\chi). \quad (30)$$

The Eq. (30) is the criterion for source detection.

4. Numerical Simulation Results

This section presents the results of the numerical modeling of the interferogram $I(\omega, t)$ and the hologram $F(\tau, \tilde{v})$ for a broadband acoustic source in a shallow-water waveguide with irregular bathymetry. In the simulated scenarios, the irregularities on the bottom are aligned along the acoustic propagation path from the source to the receiver. This results in pronounced horizontal refraction. The analysis considers how such bathymetric features influence the interferogram and hologram of the acoustic field for two different source configurations. The first configuration corresponds to a fixed source-receiver geometry (i.e., a stationary source), while the second involves a moving source that propagates over irregular bathymetry. For the latter, three types of waveguide geometry are examined: regular bathymetry, a littoral wedge, and a submarine canyon. To enable direct comparison of the effects of bathymetry across all scenarios, the initial simulation parameters are identical in each case.

Section 4 is divided into six subsections, each of which addresses a specific combination of waveguide geometry and source motion. Section 4.1 presents the numerical simulation results for a regular waveguide with a stationary source, and Section 4.2 analyzes the corresponding case with a moving source. Section 4.3 reports the modeling outcomes for a littoral wedge waveguide with a stationary source. Section 4.4 examines the effects of source motion in the same bathymetric environment. Section 4.5 provides the results obtained for a canyon-type waveguide with a stationary source. Section 4.6 discusses the modifications to the acoustic field and hologram structure observed for a moving source within the canyon geometry. This organization allows for a systematic comparison of stationary and moving source scenarios across three distinct bathymetric conditions and enables the consistent assessment of the influence of bottom topography on the interferogram and hologram.

4.1. Regular Waveguide. First Case: Non-Moving Source ($v = 0$ m/s).

Consider the regular waveguide model (Figure 2(a)). In this configuration, the waveguide is characterized by a shallow, horizontally uniform water column with a constant depth and an invariant seabed elevation. This idealized setting has long been used as a benchmark in underwater

acoustics because it provides a simplified yet rigorous framework for isolating the effects of specific environmental parameters.

The regular waveguide removes bathymetric variability as a factor, allowing researchers to investigate fundamental propagation mechanisms, assess the influence of water-column properties (e.g., sound-speed profiles), and conduct systematic sensitivity studies. Its controlled geometry also facilitates the validation of theoretical formulations and serves as a reference case for the intercomparison of numerical models, enabling consistency checks across different computational approaches. Thus, the regular waveguide plays a critical role in establishing a baseline understanding and ensuring the reliability of more complex simulations in realistic ocean environments. Furthermore, it is often used to study broadband propagation and dispersion effects, offering a baseline scenario to evaluate the temporal and frequency-dependent behavior of acoustic signals in shallow water.

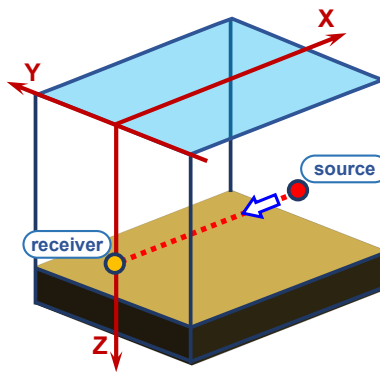


Figure 4. Model of a shallow water waveguide. Regular bathymetry.

For this geometry we have

$$z_b(\mathbf{r}) = H(\mathbf{r}) = H(x, y) = H_0, \quad (31)$$

where H_0 is the reference depth of the regular waveguide. The parameters of the regular waveguide used in the numerical simulation are presented in Table 2.

Table 2. Shallow water waveguide parameters. Regular waveguide

Parameter	$\Delta f = 100\text{--}140 \text{ Hz}$
1. Waveguide depth H_0	50 m
2. Water sound speed	1500 m/s
3. Bottom refractive index	$n_b = 0.84 (1 + i0.03)$
4. Bottom density	$\rho_b = 1.8 \text{ g/cm}^3$
5. Modes count	$M = 3$
6. Receiver coordinates	$x_q = 0, y_q = 0, z_q = 45 \text{ m}$
7. Source coordinates	$x_s = 10 \text{ km}, y_s = 0, z_s = 23 \text{ m}$
8. Source bearing	$\theta = 0^\circ$

Source coordinates: $x_s = 10 \text{ km}$, $y_s = 0 \text{ m}$, $z_s = 23 \text{ m}$. Receiver coordinates: $x_q = y_q = 0$, $z_q = 45 \text{ m}$. The source is stationary (velocity $v = 0 \text{ m/s}$) and approaching the receiver along the line $y = 0$. The initial horizontal distance between the source and the receiver is $x_0 = 10 \text{ km}$. Bearing $\theta = 0^\circ$. Frequency range $f = 100 - 140 \text{ Hz}$. Observation time $\Delta t = 300 \text{ s}$, realization duration $T = 5 \text{ s}$, time interval $\delta T = 4 \text{ s}$. Number of modes $M = 3$. Values of the propagation constants $h_m(\omega_0)$ and group velocities $u_m(\omega_0) = 1 / (\frac{dh_m(\omega_0)}{d\omega})$, $\omega = 2\pi f$, for a regular waveguide with depth $H_0 = 50 \text{ m}$ are given in Table 3. As can be seen, $h_m(\omega_0) \sim 0.49 - 0.52 \text{ m}^{-1}$ and $\frac{dh_m(\omega_0)}{d\omega} \sim 6.7 \cdot 10^4 - 7.0 \cdot 10^4 \text{ (m/s)}$.

Table 3. Sound field mode parameters ($\Delta f = 100\text{--}140\text{ Hz}$). Waveguide depth $H_0 = 50\text{ m}$.

m -th mode	h_m, m^{-1}	$(dh_m/d\omega) \cdot 10^4, (\text{m/s})^{-1}$
1	0.5164	6.6971
2	0.5071	6.7998
3	0.4908	7.0000

Figure 5 illustrates the horizontal structure of the acoustic field modes in a regular shallow-water waveguide for a stationary source ($v = 0\text{ m/s}$). Figure 5(a)–(c) show the horizontal ray trajectories for the first, second, and third modes, respectively. Figure 5(d)–(f) present the corresponding normalized horizontal amplitude distributions, where the color scale (0 to 1) indicates relative amplitude. Red dots mark the positions of the source (left) and receiver (right), which are separated by 10 km along the x -axis. A regular waveguide for sound propagation represents an isotropic propagation medium in the horizontal plane. Therefore, as illustrated in Figure 5, the ray structure and amplitude distribution correspond to the rectilinear propagation of sound waves from the source to the receiver.

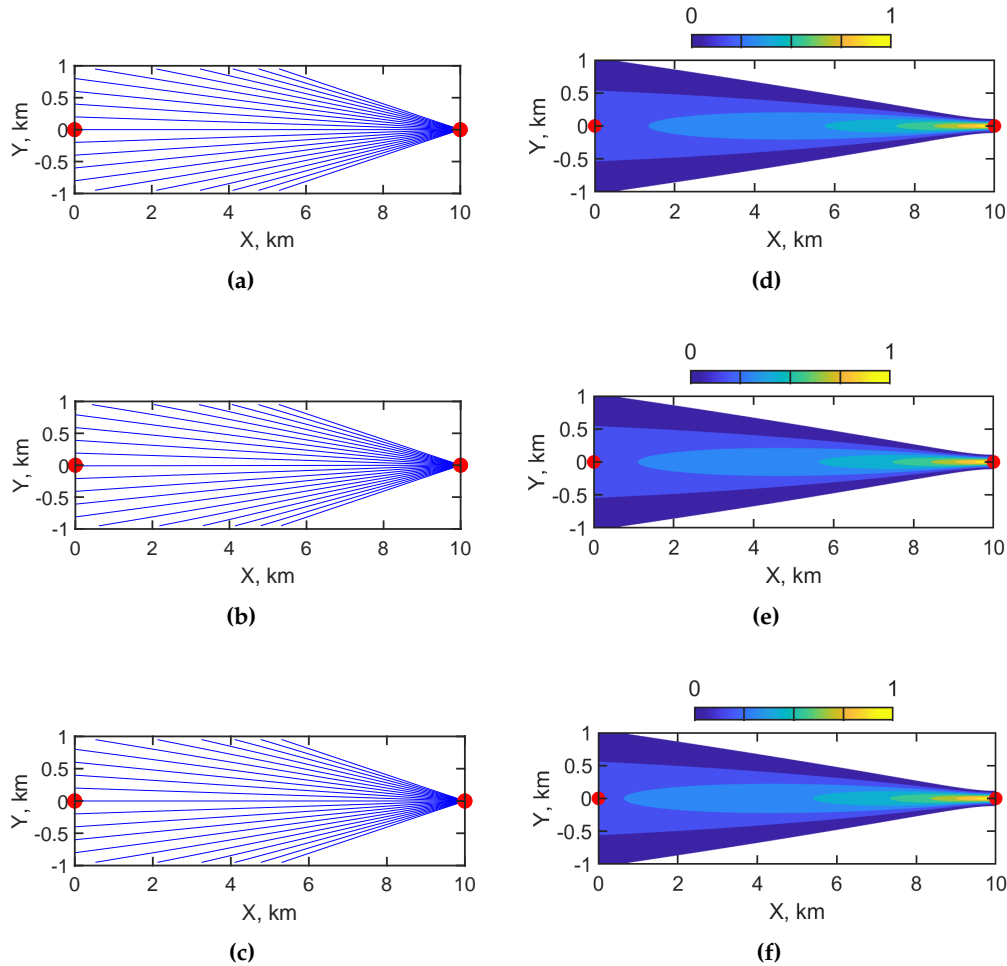


Figure 5. Horizontal structure of sound field modes: (a) horizontal rays of first mode; (b) horizontal rays of second mode; (c) horizontal rays of third mode; (d) amplitude distribution of first mode; (e) amplitude distribution of second mode; (f) amplitude distribution of third mode. Red dots indicate the source and receiver. Regular waveguide. Non-moving source ($v = 0\text{ m/s}$). Source at 10 km.

Figure 6 presents the results of the HSP method for a stationary acoustic source in a regular waveguide. Figure 6(a) shows the interferogram $I(f, t)$, where the spectral content in the 100–140 Hz band remains stable throughout the observation interval, reflecting the absence of variations due to source motion. Figure 6(b) displays the hologram $F(\tau, \tilde{v})$. As can be seen, the focal spots in the

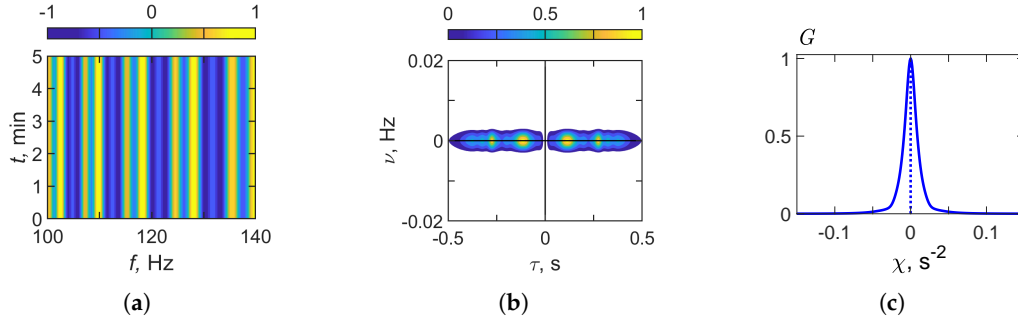


Figure 6. Results of holographic signal processing: (a) $I(f, t)$, (b) $F(\tau, \tilde{\nu})$, (c) $G(\chi)$. Regular waveguide. Non-moving source ($v = 0$ m/s). Frequency band: $\Delta f = 100 - 140$ Hz.

hologram domain for a stationary source are located along the τ -axis. Figure 6(c) illustrates the function $G(\chi)$, which exhibits a sharp, well-defined peak at $\chi = 0$, indicating the stationary of the source.

Table 4. Numerical results of holographic signal processing. Source parameters.

No.	$\Delta f = 100\text{--}140$ Hz
1.	$\delta f / \delta t \approx 0.0 \text{ s}^{-2}$
2.	$\tau_1 = 1.07 \cdot 10^{-1} \text{ s}$
3.	$\nu_1 = 0.0 \cdot 10^{-3} \text{ Hz}$
4.	$\chi = 0.0 \text{ s}^{-2}$
5.	$\dot{v} = 0.0 \text{ m/s}$
6.	$\dot{x}_0 = 10.4 \text{ km}$

Table 4 summarizes the numerical results of holographic signal processing for the frequency band $\Delta f = 100\text{--}140$ Hz. Analysis of the HSP results (see Figure 5) indicates that the rate of frequency variation of the interferogram is approximately $\delta f / \delta t \approx 0.0 \text{ s}^{-2}$. The focal point coordinates in hologram are $\tau_1 = 1.07 \cdot 10^{-1} \text{ s}$ and $\nu_1 = 0.0 \cdot 10^{-3} \text{ Hz}$. The extremum point of $G(\chi)$ is found to be $\chi = 0.0 \text{ s}^{-2}$, which is consistent with the case of a stationary source. The reconstructed source characteristics obtained from the holographic processing parameters are: velocity $\dot{v} = 0.0 \text{ m/s}$ and range $\dot{x}_0 = 10.4 \text{ km}$. The error in the reconstructed source values amounts to 0 % for the velocity and 4 % for the range.

4.2. Regular Waveguide. Second Case: Moving Source ($v = -3 \text{ m/s}$).

In this section, we present the results of holographic processing obtained through numerical modeling when the source moves within a regular waveguide. The parameters of the regular waveguide used in the numerical simulation are presented in Table 2. The numerical experiment was conducted under the following conditions. The source was located at the coordinates $x_s = 10 \text{ km}$, $y_s = 0 \text{ m}$, $z_s = 23 \text{ m}$, and the receiver was positioned at $x_q = y_q = 0$, $z_q = 45 \text{ m}$. The source propagated toward the receiver along the line $y = 0$, moving from 10 km to 9.1 km with a constant velocity of $v = -3 \text{ m/s}$. The initial horizontal separation between the source and receiver was $x_0 = 10 \text{ km}$, with a bearing of $\theta = 0^\circ$. The acoustic signal was analyzed within the frequency band $f = 100\text{--}140 \text{ Hz}$. The observation interval was $\Delta t = 300 \text{ s}$, with a realization length of $T = 5 \text{ s}$ and a temporal shift between realizations of $\delta T = 4 \text{ s}$. The field was represented using $M = 3$ modes. For a regular waveguide with a depth $H_0 = 50 \text{ m}$, the corresponding propagation constants $h_m(\omega_0)$ and group velocities $u_m(\omega_0) = 1 / \left(\frac{dh_m(\omega_0)}{d\omega} \right)$, are summarized in Table 3.

Figure 7 illustrates the horizontal structure of the acoustic field modes in a regular shallow-water waveguide for a moving source ($v = -3 \text{ m/s}$). Figure 7(a)–(c) show the horizontal ray trajectories for the first, second, and third modes, respectively, as the source moves toward the receiver. Figure 7(d)–(f) present the corresponding normalized horizontal amplitude distributions, where the color scale (0 to 1) indicates relative amplitude. The red dots indicate the source's (left, initially at $x = 9.1 \text{ km}$) and

receiver's (right, at $x = 0$) instantaneous positions, with the source approaching along the x -axis. In the case of a moving source, the regular waveguide represents an isotropic propagation medium in the horizontal plane. The overall structure of rays and amplitudes continues to reflect rectilinear propagation from the source to the receiver.

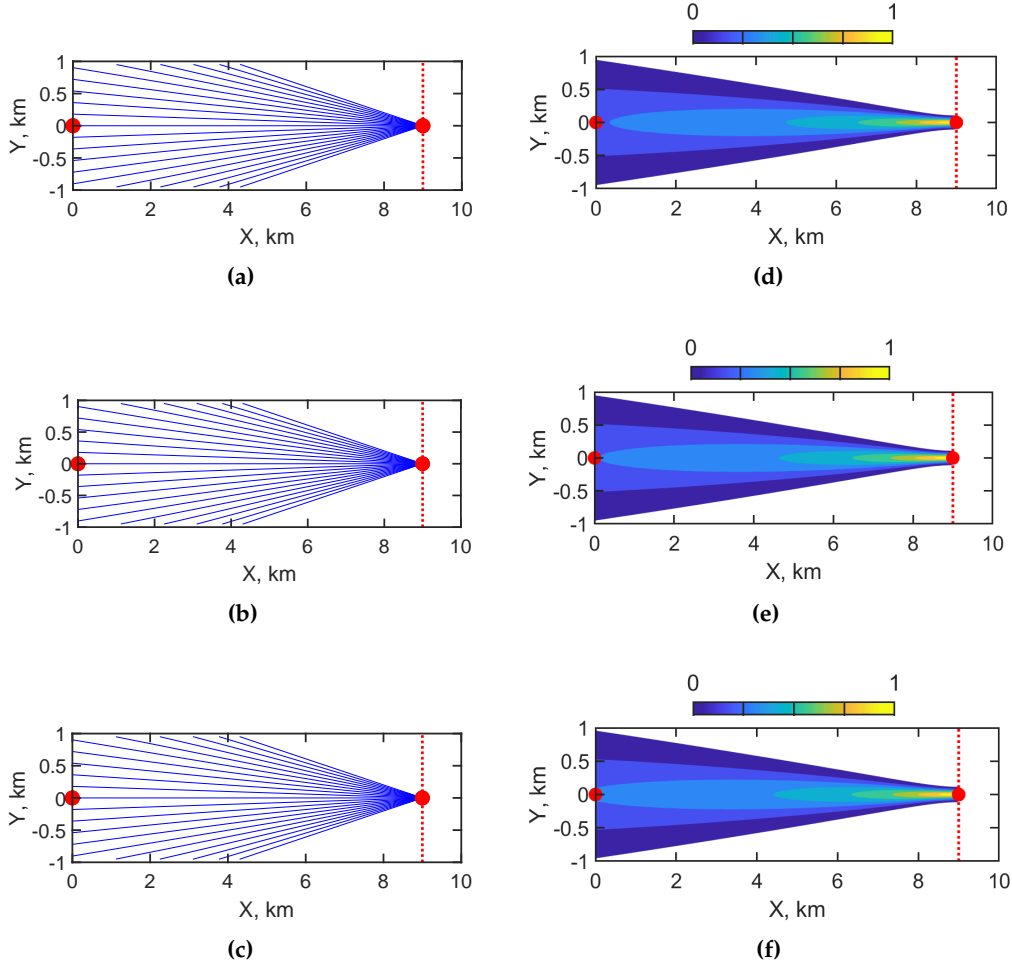


Figure 7. Horizontal structure of sound field modes: (a) horizontal rays of first mode; (b) horizontal rays of second mode; (c) horizontal rays of third mode; (d) amplitude distribution of first mode; (e) amplitude distribution of second mode; (f) amplitude distribution of third mode. Red dots indicate the source and receiver. Regular waveguide. Moving source ($v = -3$ m/s). Source moved from 10 km to 9.1 km.

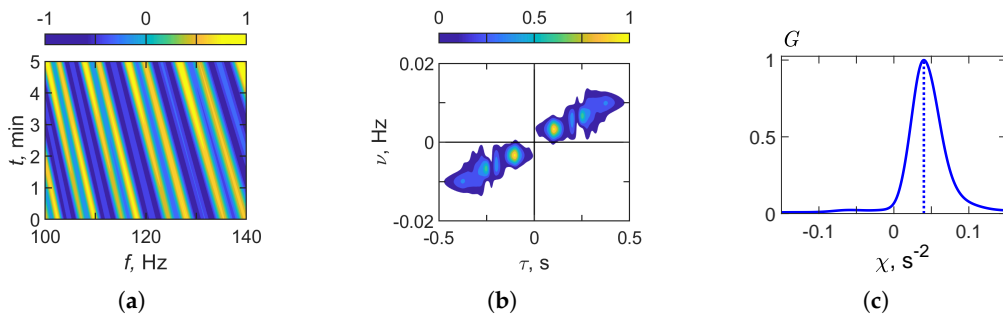


Figure 8. Results of the holographic signal processing: (a) $I(f, t)$, (b) $F(\tau, \tilde{\nu})$, (c) $G(\chi)$. Regular waveguide. Moving source ($v = -3$ m/s). Frequency band: $\Delta f = 100 - 140$ Hz.

Figure 8 presents the HSP results for a moving acoustic source in a regular waveguide ($v = -3$ m/s). Figure 8(a) shows the interferogram $I(f, t)$, where the spectral content in the band 100 –

140 Hz exhibits slanted interference fringes. These tilted structures reflect the temporal frequency variations caused by the motion of the source. Figure 8(b) displays the hologram $F(\tau, \tilde{\nu})$. Unlike the stationary case, the focal spots are shifted from the τ -axis and aligned along a non-zero frequency ν , corresponding to the source's motion toward the receiver. Figure 8(c) illustrates the function $G(\chi)$, which has a pronounced maximum at $\chi \neq 0$, thereby confirming the nonstationary character of the source.

Table 5. Interferogram and hologram structure parameters. Estimation of the source parameters.

No.	$\Delta f_1 = 100\text{--}140 \text{ Hz}$
1.	$\delta f / \delta t \approx -0.036 \text{ s}^{-2}$
2.	$\tau_1 = 1.01 \cdot 10^{-1} \text{ s}$
3.	$\nu_1 = 3.1 \cdot 10^{-3} \text{ Hz}$
4.	$\chi = 0.0375 \text{ s}^{-2}$
5.	$\dot{\nu} = -3.2 \text{ m/s}$
6.	$\dot{x}_0 = 9.8 \text{ km}$

Table 5 presents the interferogram and hologram structure parameters used to estimate source characteristics in the frequency band $\Delta f = 100 - 140 \text{ Hz}$. Analysis of the HSP results (see Figure 8) shows that the rate of frequency variation in the interferogram is approximately $\delta f / \delta t \approx -0.036 \text{ s}^{-2}$, reflecting the effect of source motion. The focal point coordinates in the hologram are determined as $\tau_1 = 1.01 \cdot 10^{-1} \text{ s}$ and $\nu_1 = 3.1 \cdot 10^{-3} \text{ Hz}$. The extremum of the function $G(\chi)$ is obtained at $\chi = 0.0375 \text{ s}^{-2}$, which corresponds to a nonstationary source. The reconstructed source parameters derived from these values are: velocity $\dot{\nu} = -3.2 \text{ m/s}$ and range $\dot{x}_0 = 9.8 \text{ km}$. The error of the reconstructed source values amounts to 7 % for the velocity and 2 % for the range.

4.3. Littoral Wedge Waveguide.

Consider the littoral wedge waveguide (see Figure 9). The littoral wedge model represents a shallow-water acoustic environment in which the depth changes linearly along one horizontal axis. Despite its simplified formulation, this configuration is a useful and widely adopted model of realistic nearshore conditions, including continental shelves, gently sloping seabeds, tidal flats, and coastal approaches. In these environments, the bathymetry gradually inclines, either deepening toward the open ocean or shoaling toward the coastline.

This representation offers a mathematically tractable and physically meaningful framework for analyzing sound propagation in coastal waters, where variations in the seafloor exert a dominant influence on acoustic field characteristics. Specifically, gradual depth changes modify propagation paths, affect group and phase velocities, and alter reflection and refraction processes at the seabed and free surface. The littoral wedge model retains the essential geometric features of sloping-bottom topographies while avoiding the complexity of fully irregular bathymetries. This enables systematic investigations of shallow-water acoustic phenomena under controlled and reproducible conditions. Thus, it offers valuable insights into real-world applications of underwater acoustics.

In this case we have

$$z_b(\mathbf{r}) = H(\mathbf{r}) = H(x, y) = H_0 - k_0 y. \quad (32)$$

where H_0 is the reference depth, k_0 is slope coefficient. The parameters of the littoral wedge used in the numerical simulation are presented in Table 6.

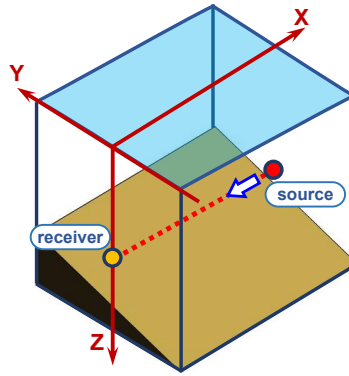


Figure 9. Model of a shallow water waveguide. Littoral wedge.

Table 6. Shallow water waveguide parameters. Littoral wedge waveguide.

Parameter	$\Delta f = 100 - 140 \text{ Hz}$
1. Waveguide depth H_0	50 m
2. Slope coefficient	$k_0 = 0.01$
3. Water sound speed	1500 m/s
4. Bottom refractive index	$n_b = 0.84 (1 + i0.03)$
5. Bottom density	$\rho_b = 1.8 \text{ g/cm}^3$
6. Modes count	$M = 3$
7. Receiver coordinates	$x_q = 0, y_q = 0, z_q = 45 \text{ m}$
8. Source coordinates	$x_s = 10 \text{ km}, y_s = 0, z_s = 23 \text{ m}$
9. Source bearing	$\theta = 0^\circ$

Source coordinates: $x_s = 10 \text{ km}$, $y_s = 0 \text{ m}$, $z_s = 23 \text{ m}$. Receiver coordinates: $x_q = y_q = 0$, $z_q = 45 \text{ m}$. The source is stationary (velocity $v = 0 \text{ m/s}$) and approaching the receiver along the line $y = 0$. The initial horizontal distance between the source and the receiver is $x_0 = 10 \text{ km}$. Bearing $\theta = 0^\circ$. Frequency range $f = 100 - 140 \text{ Hz}$. Observation time $\Delta t = 300 \text{ s}$, realization duration $T = 5 \text{ s}$, time interval $\delta T = 4 \text{ s}$. Number of modes $M = 3$. Values of the propagation constants $h_m(\omega_0)$ and group velocities $u_m(\omega_0) = 1 / (\frac{dh_m(\omega_0)}{d\omega})$, $\omega = 2\pi f$, for a littoral wedge waveguide are given in Table 7, Table 8, Table 9. Table 7 corresponds to depth $H_0 = 50 \text{ m}$, $h_m(\omega_0) \sim 0.49 - 0.52 \text{ m}^{-1}$ and $\frac{dh_m(\omega_0)}{d\omega} \sim 6.7 \cdot 10^4 - 7.0 \cdot 10^4 (\text{m/s})^{-1}$. Table 8 corresponds to depth $H = H_0 - 10 = 40 \text{ m}$, $h_m(\omega_0) \sim 0.47 - 0.51 \text{ m}^{-1}$ and $\frac{dh_m(\omega_0)}{d\omega} \sim 6.7 \cdot 10^4 - 7.2 \cdot 10^4 (\text{m/s})^{-1}$. Table 9 corresponds to depth $H = H_0 + 10 = 60 \text{ m}$, $h_m(\omega_0) \sim 0.50 - 0.52 \text{ m}^{-1}$ and $\frac{dh_m(\omega_0)}{d\omega} \sim 6.7 \cdot 10^4 - 6.9 \cdot 10^4 (\text{m/s})^{-1}$.

Table 7. Sound field mode parameters ($\Delta f = 100\text{--}140 \text{ Hz}$). Waveguide depth $H_0 = 50 \text{ m}$.

m -th mode	h_m, m^{-1}	$(dh_m/d\omega) \cdot 10^4, (\text{m/s})^{-1}$
1	0.5164	6.6971
2	0.5071	6.7998
3	0.4908	7.0000

Table 8. Sound field mode parameters ($\Delta f = 100\text{--}140 \text{ Hz}$). Waveguide depth $H = H_0 - 10 = 40 \text{ m}$.

m -th mode	h_m, m^{-1}	$(dh_m/d\omega) \cdot 10^4, (\text{m/s})^{-1}$
1	0.5149	6.710
2	0.5009	6.864
3	0.4757	7.182

Table 9. Sound field mode parameters ($\Delta f = 100\text{--}140\text{ Hz}$). Waveguide depth $H = H_0 + 10 = 60\text{ m}$.

m -th mode	h_m, m^{-1}	$(dh_m/d\omega) \cdot 10^4, (\text{m/s})^{-1}$
1	0.5172	6.689
2	0.5106	6.763
3	0.4992	6.901

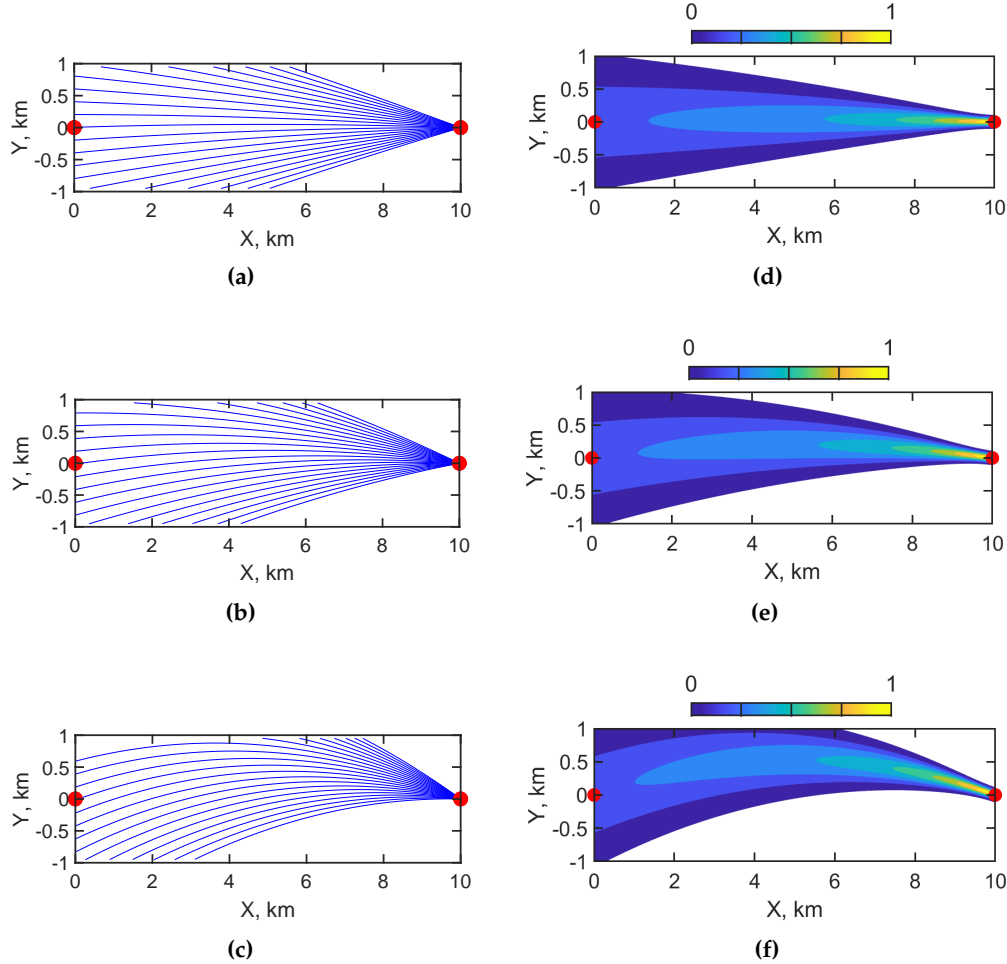


Figure 10. Horizontal structure of the sound field modes: (a) horizontal rays of first mode; (b) horizontal rays of second mode; (c) horizontal rays of third mode; (d) amplitude distribution of first mode; (e) amplitude distribution of second mode; (f) amplitude distribution of third mode. Red dots indicate the source and receiver. Littoral wedge waveguide. Non-moving source ($v = 0\text{ m/s}$). Source at 10 km.

Figure 10 illustrates the horizontal structure of the acoustic field modes in a littoral wedge waveguide for a stationary source ($v = 0\text{ m/s}$) located at $x = 10\text{ km}$. Figures 10(a)–(c) show the horizontal ray trajectories corresponding to the first, second, and third modes, respectively. Figures 10(d)–(f) present the associated normalized horizontal amplitude distributions, where the color scale (0 to 1) indicates relative amplitude. The red dots mark the positions of the source (right) and the receiver (left) along the x -axis. Unlike in a regular waveguide, the presence of sloping bathymetry in a wedge environment leads to the horizontal refraction of acoustic modes. This is evident in the curvature of the ray paths and the asymmetry of the amplitude distributions.

Figure 11 presents the results of the HSP method for a stationary acoustic source in a littoral wedge waveguide. Figure 11(a) shows the interferogram $I(f, t)$, where the spectral content in the 100–140 Hz band remains stable throughout the observation interval, consistent with the absence of source motion. Figure 11(b) displays the hologram $F(\tau, \nu)$. The focal spots in the hologram domain

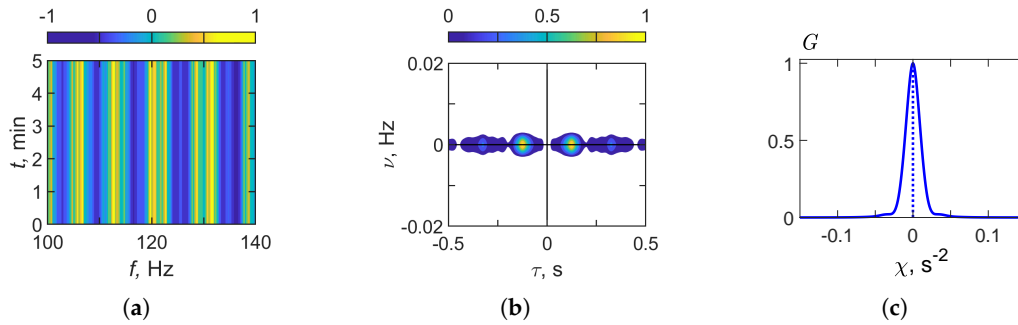


Figure 11. Results of holographic signal processing: (a) $I(f, t)$, (b) $F(\tau, \tilde{\nu})$, (c) $G(\chi)$. Littoral wedge waveguide. Non-moving source ($v = 0$ m/s). Frequency band: $\Delta f = 100 - 140$ Hz.

are aligned along the τ -axis, indicating the stationary nature of the source. Figure 11(c) illustrates the function $G(\chi)$, which has a sharp, well-defined maximum at $\chi = 0$. This confirms the absence of motion and validates the stability of the reconstructed parameters in the wedge environment.

Table 10. Interferogram and hologram structure parameters. Estimation of the source parameters.

No.	$\Delta f = 100\text{--}140$ Hz
1.	$\delta f / \delta t \approx 0.0 \text{ s}^{-2}$
2.	$\tau_1 = 1.12 \cdot 10^{-1} \text{ s}$
3.	$\nu_1 = 0.0 \cdot 10^{-3} \text{ Hz}$
4.	$\chi = 0.0 \text{ s}^{-2}$
5.	$\dot{v} = 0.0 \text{ m/s}$
6.	$\dot{x}_0 = 10.7 \text{ km}$

Table 10 summarizes the interferogram and hologram structure parameters obtained from HSP in the frequency band $\Delta f = 100\text{--}140$ Hz. Analysis of the results (see Figure 11) shows that the rate of frequency variation in the interferogram is approximately $\delta f / \delta t \approx 0.0 \text{ s}^{-2}$, indicating the absence of frequency modulation. The focal point coordinates in the hologram are determined as $\tau_1 = 1.12 \cdot 10^{-1} \text{ s}$ and $\nu_1 = 0.0 \cdot 10^{-3} \text{ Hz}$. The extremum of the function $G(\chi)$ is found at $\chi = 0.0 \text{ s}^{-2}$, which is consistent with the case of a stationary source. The reconstructed source parameters derived from these values are: velocity $\dot{v} = 0.0 \text{ m/s}$ and range $\dot{x}_0 = 10.7 \text{ km}$. The error of the reconstructed estimates is 0 % for the velocity and approximately 7 % for the range, confirming the accuracy and robustness of holographic processing in the littoral wedge waveguide for a stationary source.

4.4. Littoral Wedge Waveguide. Second Case: Moving Source ($v = -3 \text{ m/s}$).

In this section, we present the results of holographic processing obtained through numerical modeling for the case of a source moving in a littoral wedge waveguide. The parameters of the wedge-shaped environment used in the simulations are summarized in Table 2. The numerical experiment was carried out under the following conditions. The source was initially located at coordinates $x_s = 10 \text{ km}$, $y_s = 0 \text{ m}$, $z_s = 23 \text{ m}$, while the receiver was positioned at $x_q = y_q = 0$, $z_q = 45 \text{ m}$. The source propagated toward the receiver along the line $y = 0$, moving from $x = 10 \text{ km}$ to $x = 9.1 \text{ km}$ with a constant velocity of $v = -3 \text{ m/s}$. The initial horizontal separation between the source and the receiver was $x_0 = 10 \text{ km}$, with a bearing of $\theta = 0^\circ$. The acoustic signal was analyzed within the frequency band $f = 100\text{--}140 \text{ Hz}$. The observation interval was $\Delta t = 300 \text{ s}$, with a realization length of $T = 5 \text{ s}$ and a temporal shift between realizations of $\delta T = 4 \text{ s}$. The field was represented using $M = 3$ modes. The corresponding propagation constants $h_m(\omega_0)$ and group velocities $u_m(\omega_0) = 1 / (\frac{dh_m(\omega_0)}{d\omega})$ are provided in Table 7, Table 8, Table 9.

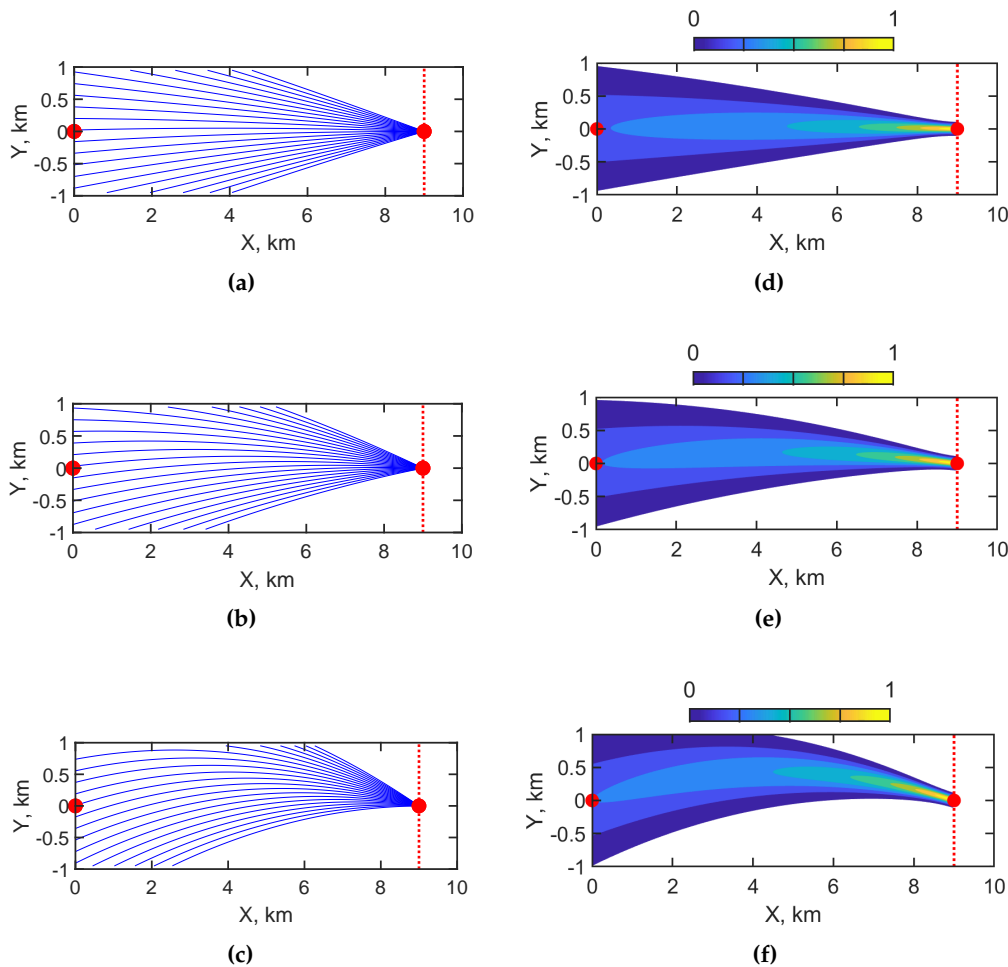


Figure 12. Horizontal structure of sound field modes: (a) horizontal rays of first mode; (b) horizontal rays of second mode; (c) horizontal rays of third mode; (d) amplitude distribution of first mode; (e) amplitude distribution of second mode; (f) amplitude distribution of third mode. Red dots indicate the source and the receiver. Littoral wedge waveguide. Moving source ($v = -3$ m/s). Source moved from 10 km to 9.1 km.

Figure 12 illustrates the horizontal structure of the acoustic field modes in a littoral wedge waveguide for a moving source ($v = -3$ m/s). Figures 12(a)–(c) display the horizontal ray trajectories for the first, second, and third modes, respectively, as the source moves toward the receiver. Figures 12(d)–(f) show the corresponding normalized horizontal amplitude distributions, with the color scale (0 to 1) indicating relative amplitude. The red dots indicate the instantaneous positions of the source (left, at $x = 9.1$ km) and the receiver (right, at $x = 0$), with the source moving along the x -axis. In the case of a moving source in a wedge-shaped environment, horizontal propagation becomes range-dependent due to varying depths. The structure of the rays and amplitudes reflects the influence of sloping bathymetry on the distribution of modal energy and the source's approach to the receiver.

Figure 13 presents the results of holographic signal processing for a moving source in a littoral wedge waveguide ($v = -3$ m/s). Figure 13(a) shows the interferogram $I(f, t)$ within the frequency band 100–140 Hz, where inclined interference fringes are observed. These oblique patterns indicate frequency-time modulation induced by the source motion. Figure 13(b) depicts the hologram $F(\tau, \nu)$, where the focal regions are displaced from the τ -axis and distributed along a non-zero frequency ν , consistent with a source approaching the receiver. Finally, Figure 13(c) illustrates the function $G(\chi)$, which exhibits a distinct peak at $\chi \neq 0$, thereby confirming the nonstationary dynamics of the source.

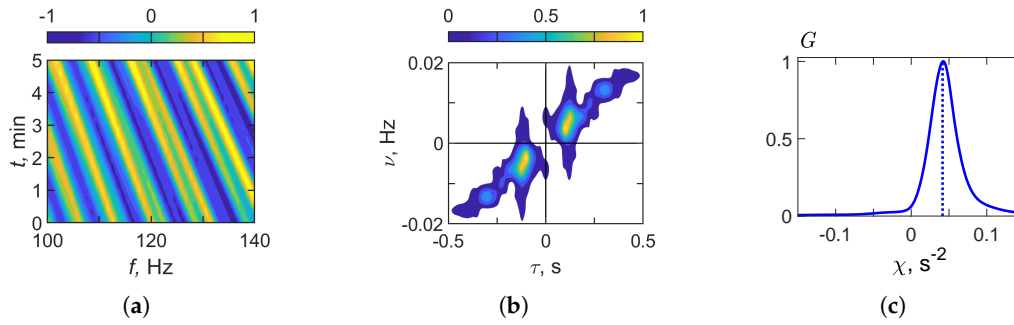


Figure 13. Results of holographic signal processing: (a) $I(f, t)$, (b) $F(\tau, \tilde{\nu})$, (c) $G(\chi)$. Littoral wedge waveguide. Moving source ($v = -3$ m/s). Frequency band: $\Delta f = 100 - 140$ Hz.

Table 11. Interferogram and hologram structure parameters. Estimation of the source parameters.

No.	$\Delta f = 100\text{--}140$ Hz
1.	$\delta f / \delta t \approx -0.038 \text{ s}^{-2}$
2.	$\tau_1 = 1.01 \cdot 10^{-1} \text{ s}$
3.	$\nu_1 = 3.2 \cdot 10^{-3} \text{ Hz}$
4.	$\chi = 0.039 \text{ s}^{-2}$
5.	$\dot{v} = -3.4 \text{ m/s}$
6.	$\dot{x}_0 = 9.8 \text{ km}$

Table 11 summarizes the interferogram and hologram structure parameters derived from holographic signal processing in the frequency band $\Delta f = 100\text{--}140$ Hz. As shown in Figure 13, the frequency variation rate in the interferogram is estimated to be approximately $\delta f / \delta t \approx -0.038 \text{ s}^{-2}$, indicating noticeable frequency modulation caused by the moving source. The focal spot coordinates in the hologram are determined to be $\tau_1 = 1.01 \cdot 10^{-1} \text{ s}$ and $\nu_1 = 3.2 \cdot 10^{-3} \text{ Hz}$. The function $G(\chi)$ exhibits a pronounced maximum at $\chi = 0.039 \text{ s}^{-2}$, further confirming the nonstationary nature of the source. Based on these results, the reconstructed source parameters are velocity $\dot{v} = -3.4 \text{ m/s}$ and range $\dot{x}_0 = 9.8 \text{ km}$. The error in the reconstructed estimates is 13% for velocity and approximately 2% for range, confirming the accuracy and robustness of holographic processing in the littoral wedge waveguide for a moving source.

4.5. Canyon Waveguide. First Case: Non-Moving Source ($v = 0 \text{ m/s}$)

Consider the canyon waveguide (see Figure 14). This model represents an oceanic environment characterized by a sharp depression with steeply sloping sides and a relatively narrow cross-section. Though idealized, this configuration captures the essential features of submarine canyons, which are prominent topographic features that connect shallow continental shelves to deeper ocean basins. These environments are of particular interest in underwater acoustics because of their strong influence on sound propagation, scattering, and trapping mechanisms.

The canyon's geometry significantly modifies acoustic field characteristics. Steep bathymetric gradients, in particular, induce mode coupling, generate shadowing effects, and enhance multipath propagation. The canyon walls can also act as acoustic waveguides, channeling energy along the axis of the depression while altering reflection and refraction conditions compared to flat-bottomed or wedge-like topographies. These effects make the canyon waveguide a useful model for analyzing the complex interactions between bathymetric structure and acoustic propagation.

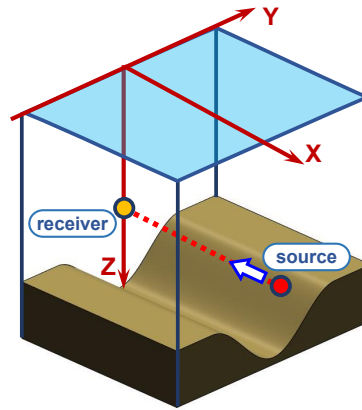


Figure 14. Model of shallow water waveguide. Canyon.

The mathematical model of the canyon waveguide bathymetry has the following form:

$$H(\mathbf{r}) = H(x, y) = H_0 + A_0 \text{sech}^2(y/L_0), \quad (33)$$

where H_0 is the reference depth, A_0 is canyon depth, L_0 is canyon half-width. The parameters of the littoral wedge used in the numerical simulation are presented in Table 12.

Table 12. Shallow water waveguide parameters. Littoral wedge waveguide.

Parameter	$\Delta f = 100\text{--}140 \text{ Hz}$
1. Waveguide depth H_0	50 m
2. Canyon depth	$A_0 = 10 \text{ m}$
3. Canyon half-width	$L_0 = 300 \text{ m}$
4. Water sound speed	1500 m/s
5. Bottom refractive index	$n_b = 0.84 (1 + i0.03)$
6. Bottom density	$\rho_b = 1.8 \text{ g/cm}^3$
7. Modes count	$M = 3$
8. Receiver coordinates	$x_q = 0, y_q = 0, z_q = 45 \text{ m}$
9. Source coordinates	$x_s = 10 \text{ km}, y_s = 0, z_s = 23 \text{ m}$
10. Source bearing	$\theta = 0^\circ$

Source coordinates: $x_s = 10 \text{ km}, y_s = 0 \text{ m}, z_s = 23 \text{ m}$. Receiver coordinates: $x_q = y_q = 0, z_q = 45 \text{ m}$. The source is stationary (velocity $v = 0 \text{ m/s}$) and approaching the receiver along the line $y = 0$. The initial horizontal distance between the source and the receiver is $x_0 = 10 \text{ km}$. Bearing $\theta = 0^\circ$. Frequency range $f = 100 - 140 \text{ Hz}$. Observation time $\Delta t = 300 \text{ s}$, realization duration $T = 5 \text{ s}$, time interval $\delta T = 4 \text{ s}$. Number of modes $M = 3$. Values of the propagation constants $h_m(\omega_0)$ and group velocities $u_m(\omega_0) = 1 / (\frac{dh_m(\omega_0)}{d\omega})$, $\omega = 2\pi f$, for a littoral wedge waveguide are given in Table 13, Table 14. Table 13 is corresponding to depth $H_0 = 50 \text{ m}$, $h_m(\omega_0) \sim 0.49 - 0.52 \text{ m}^{-1}$ and $\frac{dh_m(\omega_0)}{d\omega} \sim 6.7 \cdot 10^4 - 7.0 \cdot 10^4 (\text{m/s})^{-1}$. Table 14 is corresponding to depth $H = H_0 + A_0 = 60 \text{ m}$, $h_m(\omega_0) \sim 0.50 - 0.52 \text{ m}^{-1}$ and $\frac{dh_m(\omega_0)}{d\omega} \sim 6.7 \cdot 10^4 - 6.9 \cdot 10^4 (\text{m/s})^{-1}$.

Table 13. Sound field mode parameters ($\Delta f = 100\text{--}140 \text{ Hz}$). Waveguide depth $H_0 = 50 \text{ m}$.

m -th mode	h_m, m^{-1}	$(dh_m/d\omega) \cdot 10^4, (\text{m/s})^{-1}$
1	0.5164	6.6971
2	0.5071	6.7998
3	0.4908	7.0000

Figure 15 shows the horizontal structure of acoustic field modes in a canyon waveguide for a stationary source ($v = 0 \text{ m/s}$) positioned at $x = 10 \text{ km}$. Figures 15(a)–(c) display the horizontal

Table 14. Sound field mode parameters ($\Delta f = 100\text{--}140\text{ Hz}$). Waveguide depth $H = H_0 + A_0 = 60\text{ m}$.

m -th mode	h_m, m^{-1}	$(dh_m/d\omega) \cdot 10^4, (\text{m/s})^{-1}$
1	0.5172	6.689
2	0.5106	6.763
3	0.4992	6.901

ray trajectories for the first, second, and third modes, respectively. Figures 15(d)–(f) present the corresponding normalized horizontal amplitude distributions, with the color scale ranging from 0 to 1 indicating relative amplitude. The source and receiver positions are marked by red dots on the x -axis. Unlike the wedge geometry, the canyon topography produces strong horizontal refraction and mode confinement. This is evident in the bending of ray paths and the localized concentration of acoustic energy within the canyon region.

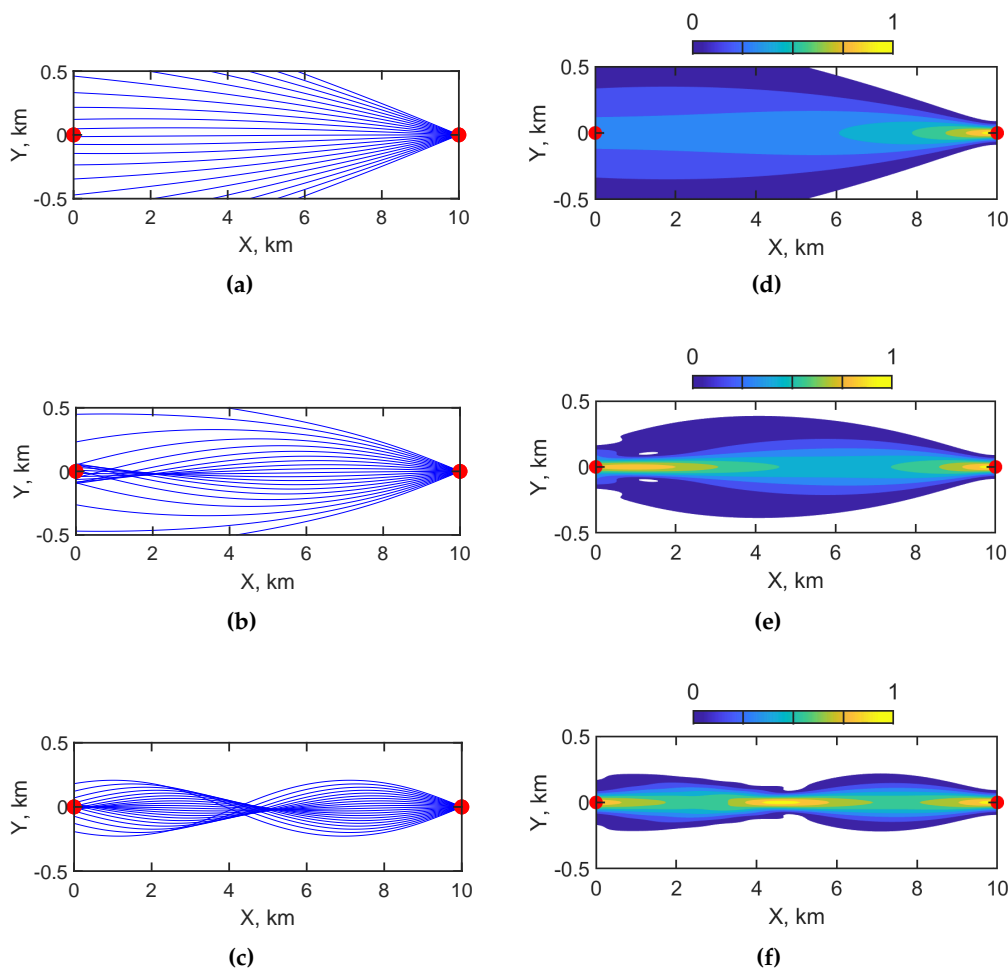


Figure 15. Horizontal structure of sound field modes: (a) horizontal rays of first mode; (b) horizontal rays of second mode; (c) horizontal rays of third mode; (d) amplitude distribution of first mode; (e) amplitude distribution of second mode; (f) amplitude distribution of third mode. Red dots indicate the source and the receiver. Canyon waveguide. Non-moving source ($v = 0\text{ m/s}$). Source at 10 km.

Figure 16 presents the results of holographic signal processing for a stationary acoustic source in a canyon waveguide. Figure 16(a) shows the interferogram $I(f, t)$, in which the spectral content within the 100–140 Hz frequency band remains constant over time. This indicates an absence of frequency modulation due to source motion. Figure 16(b) depicts the hologram $F(\tau, \nu)$, in which the focal spots are concentrated along the τ -axis, consistent with a stationary source. Figure 16(c) shows the function

$G(\chi)$, which has a clear peak at $\chi = 0$. This confirms that the source is not moving and validates the stability of the reconstructed parameters in the canyon environment.

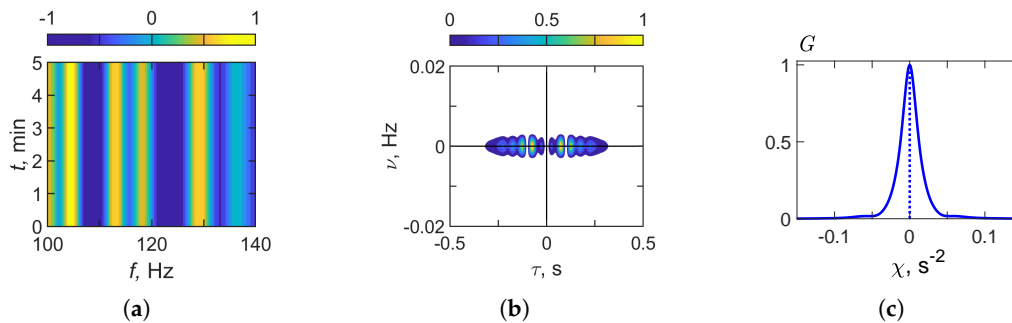


Figure 16. Results of holographic signal processing: (a) $I(f, t)$, (b) $F(\tau, \tilde{\nu})$, (c) $G(\chi)$. Canyon waveguide. Non-moving source ($v = 0$ m/s). Frequency band: $\Delta f = 100 - 140$ Hz.

Table 15. Interferogram and hologram structure parameters. Estimation of source parameters.

No.	$\Delta f = 100\text{--}140$ Hz
1.	$\delta f / \delta t \approx -0.0 \text{ s}^{-2}$
2.	$\tau_1 = 0.78 \cdot 10^{-1} \text{ s}$
3.	$\nu_1 = 0.0 \cdot 10^{-3} \text{ Hz}$
4.	$\chi = 0.0 \text{ s}^{-2}$
5.	$\dot{v} = 0.0 \text{ m/s}$
6.	$\dot{x}_0 = 10.5 \text{ km}$

Table 15 summarizes the interferogram and hologram structure parameters obtained from holographic signal processing in the frequency band $\Delta f = 100\text{--}140$ Hz. The analysis of the results (see Figure 16) shows that the frequency variation rate in the interferogram is $\delta f / \delta t \approx 0.0 \text{ s}^{-2}$, confirming the absence of modulation effects associated with source motion. The focal spot coordinates in the hologram are found to be $\tau_1 = 0.78 \cdot 10^{-1} \text{ s}$ and $\nu_1 = 0.0 \cdot 10^{-3} \text{ Hz}$. The function $G(\chi)$ reaches its maximum at $\chi = 0.0 \text{ s}^{-2}$, which is consistent with the stationary nature of the source. The reconstructed parameters derived from these values are: velocity $\dot{v} = 0.0 \text{ m/s}$ and range $\dot{x}_0 = 10.5 \text{ km}$. The error of the reconstructed estimates is 0 % for the velocity and approximately 5 % for the range, confirming the accuracy and robustness of holographic processing in the canyon waveguide for a stationary source.

4.6. Canyon Waveguide. Second Case: Moving Source ($v = -3 \text{ m/s}$)

In this section, we present the results of holographic processing obtained through numerical modeling for the case of a source located in a canyon waveguide. The parameters of the canyon environment used in the simulations are summarized in Table 2. The numerical experiment was conducted under the following conditions. The source was positioned at coordinates $x_s = 10 \text{ km}$, $y_s = 0 \text{ m}$, $z_s = 23 \text{ m}$, while the receiver was positioned at $x_q = y_q = 0$, $z_q = 45 \text{ m}$. The source remained stationary ($v = 0 \text{ m/s}$) at a horizontal distance of $x_0 = 10 \text{ km}$ from the receiver, with a bearing angle of $\theta = 0^\circ$. The acoustic signal was analyzed in the frequency band $f = 100\text{--}140 \text{ Hz}$. The observation interval was $\Delta t = 300 \text{ s}$, with a realization length of $T = 5 \text{ s}$ and a temporal shift between realizations of $\delta T = 4 \text{ s}$. The acoustic field was represented using $M = 3$ modes. The corresponding propagation constants $h_m(\omega_0)$ and group velocities $u_m(\omega_0) = 1 / (\frac{dh_m(\omega_0)}{d\omega})$ are provided in Tables 13 and 14.

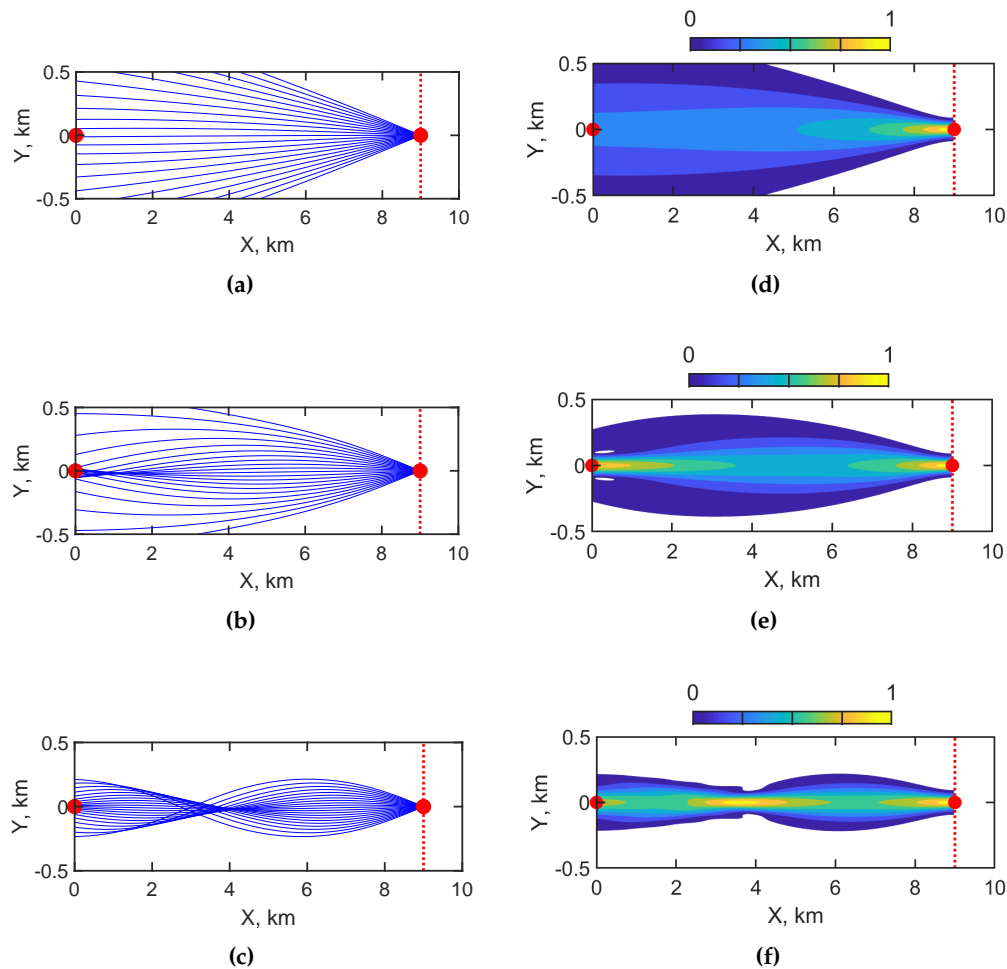


Figure 17. Horizontal structure of sound field modes: (a) horizontal rays of first mode; (b) horizontal rays of second mode; (c) horizontal rays of third mode; (d) amplitude distribution of first mode; (e) amplitude distribution of second mode; (f) amplitude distribution of third mode. Red dots indicate the source and receiver. Canyon waveguide. Moving source ($v = -3$ m/s). Source moved from 10 km to 9.1 km.

Figure 17 illustrates the horizontal structure of the acoustic field modes in a canyon waveguide for a moving source ($v = -3$ m/s). Figures 17(a)–(c) show the horizontal ray trajectories of the first, second, and third modes, respectively, as the source moves toward the receiver. Figures 17(d)–(f) display the corresponding normalized horizontal amplitude distributions, with the color scale (0 to 1) representing relative amplitude. Red dots mark the source's (left, at $x = 9.1$ km) and receiver's (right, at $x = 0$ km) instantaneous positions as the source moves along the x -axis. In the canyon environment, horizontal propagation exhibits pronounced range dependence due to steep bathymetric gradients. Both the ray structures and amplitude patterns reveal strong refraction and confinement effects that influence modal energy distribution as the source approaches the receiver.

Figure 18 presents the results of holographic signal processing for a moving source in a canyon waveguide ($v = -3$ m/s). Figure 18(a) shows the interferogram $I(f, t)$ in the frequency band 100–140 Hz, where the slanted interference fringes clearly reflect the frequency-time modulation produced by the source motion. Figure 18(b) displays the hologram $F(\tau, \tilde{\nu})$, in which the focal spots are shifted away from the τ -axis and aligned along a non-zero frequency ν , consistent with the source approaching the receiver. Figure 18(c) illustrates the function $G(\chi)$, which has a pronounced maximum at $\chi \neq 0$, thereby confirming the nonstationary character of the source in the canyon environment.

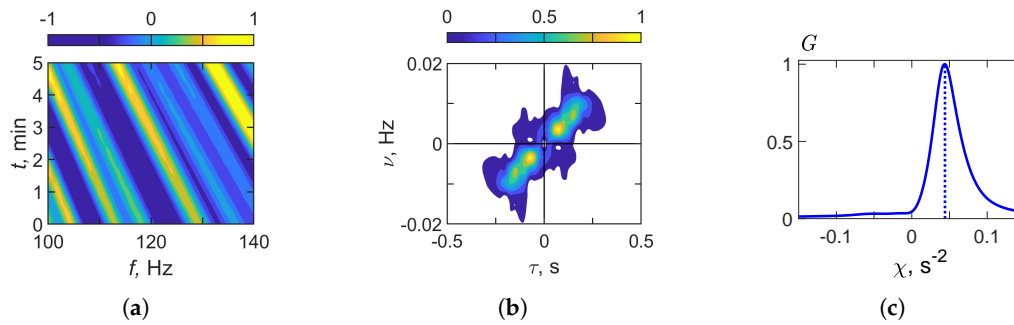


Figure 18. Results of holographic signal processing: (a) $I(f, t)$, (b) $F(\tau, \tilde{\nu})$, (c) $G(\chi)$. Canyon waveguide. Moving source ($v = -3$ m/s). Frequency band: $\Delta f = 100 - 140$ Hz.

Table 16. Interferogram and hologram structure parameters. Estimation of source parameters.

No.	$\Delta f = 100\text{--}140$ Hz
1.	$\delta f / \delta t \approx -0.038 \text{ s}^{-2}$
2.	$\tau_1 = 0.8 \cdot 10^{-1} \text{ s}$
3.	$\nu_1 = 3.3 \cdot 10^{-3} \text{ Hz}$
4.	$\chi = 0.04 \text{ s}^{-2}$
5.	$\dot{v} = -3.5 \text{ m/s}$
6.	$\dot{x}_0 = 10.8 \text{ km}$

Table 16 summarizes the interferogram and hologram structure parameters obtained from holographic signal processing in the frequency band $\Delta f = 100\text{--}140$ Hz. Figure 18 shows that the frequency variation rate in the interferogram is $\delta f / \delta t \approx -0.038 \text{ s}^{-2}$, reflecting the modulation induced by the source motion. The focal spot coordinates in the hologram are identified as $\tau_1 = 0.8 \cdot 10^{-1} \text{ s}$ and $\nu_1 = 3.3 \cdot 10^{-3} \text{ Hz}$. The function $G(\chi)$ reaches its maximum at $\chi = 0.04 \text{ s}^{-2}$, thereby confirming the nonstationary character of the source. Based on these results, the reconstructed source parameters are: velocity $\dot{v} = -3.5 \text{ m/s}$ and range $\dot{x}_0 = 10.8 \text{ km}$. The error of the reconstructed estimates is 17 % for the velocity and approximately 8 % for the range, confirming the accuracy and robustness of holographic processing in the canyon waveguide for a stationary source.

5. Conclusions

This study examined the impact of irregular bathymetry on the HSP of a moving acoustic source in a shallow-water waveguide. Using the VMHR and VMMPE approaches, we developed a source hologram model that accounts for horizontal refraction caused by irregular bathymetry. A comparative analysis of holographic processing results was carried out based on this approach for three types of waveguides: regular, littoral wedge, and canyon. This analysis enables a systematic comparison of their influence on interferograms, holograms, and reconstructed source parameters.

The results lead to the following key conclusions:

Robustness of Interferogram and Hologram Structure Under Irregular Bathymetry. Despite the significant distortion of the acoustic field's structure in the horizontal plane caused by horizontal refraction due to bathymetric variability, the interferogram and hologram retain the structural features observed in a regular waveguide. This stability ensures the preservation of the key information necessary for reconstructing source parameters, including range and velocity.

Accuracy of Source Parameter Reconstruction. Quantitative estimates show that the range of the acoustic source can be reconstructed with an error of about 10 %. For a regular waveguide, the error in velocity and range is 0 % and 4 % for a stationary source and 7 % and 2 % for a moving source, respectively. For a littoral wedge waveguide, reconstruction errors are 0 % in velocity and 7 % in range for a stationary source and 13 % and 2 %, respectively, for a moving source. In a canyon waveguide, estimation errors amount to 0 % and 5 % for velocity and range in the stationary case and 8 % and

17 % in the moving case. These levels of accuracy are sufficient for practical underwater monitoring applications.

Effectiveness of the HSP method. Comparing different waveguide types (regular, littoral wedge, and canyon) shows that bathymetric irregularities lead to only a minor increase in reconstruction errors relative to a regular waveguide. These results confirm the robustness of the holographic signal processing method and its ability to provide reliable results in realistic, shallow-water conditions with irregular bottom topography.

These findings substantially extend the applicability of holographic methods in underwater acoustics, demonstrating their potential for practical use in real-world scenarios with irregular and complex bathymetry. Furthermore, the approach's ability to provide stable parameter estimates closely aligned with actual physical values underscores its relevance for theoretical studies and operational tasks in ocean monitoring and surveillance.

6. Future Works

In previous studies, we examined sound field interferograms and holograms of a moving source in the presence of internal waves inducing horizontal refraction and mode coupling [28,29]. The primary focus of the present study was the influence of bottom relief, which causes significant horizontal refraction. It is important to note that other environmental factors also contribute to variability in the acoustic field under shallow-water conditions. Future research will extend the analysis in several directions.

Surface wave influence. We will investigate how surface gravity waves influence interferogram and hologram stability, as well as the accuracy of reconstructed source parameters. Surface wave-induced fluctuations are expected to introduce additional distortions in the interferogram, which may affect hologram focusing.

Combined variability scenarios. Future simulations will consider environments in which internal waves, bathymetric irregularities, and surface waves act simultaneously. This will provide a more realistic assessment of the robustness of holographic processing under operational conditions.

Addressing these aspects will enable subsequent studies to provide a comprehensive understanding of the stability limits of holographic signal processing in complex ocean environments, advancing its potential for operational applications in ocean acoustics.

Author Contributions: Supervision and project administration, M.E. and S.P.; conceptualization and methodology, V.K. and S.P.; software, S.T., A.P., and N.L.; validation, M.E. and V.K.; formal analysis, M.E. and S.P.; writing – original draft preparation, M.E. and S.P.; writing – review and editing, M.E. and S.P.; All authors have read and agreed to the published version of the manuscript.

Funding: This work was supported by grant from the Russian Science Foundation № 23-61-10024, <https://rscf.ru/project/23-61-10024/>.

Data Availability Statement: The original data used in the study are openly available.

Conflicts of Interest: The authors declare no conflicts of interest.

Abbreviations

The following abbreviations are used in this manuscript:

HSP	holographic signal processing;
ISP	interferometric signal processing;
3DHE	3D Helmholtz Equation models;
3DPE	3D Parabolic Equation models;
3DR	3D Ray-based models;
VMMPE	Vertical Modes and 2D Modal Parabolic Equation models;
VCMHR	Vertical Coupled Modes with Horizontal Rays models;
IIW	intense internal wave;
2D	two-dimensional;
3D	three-dimensional;
1D-FT	one-dimensional Fourier transform;
2D-FT	two-dimensional Fourier transform.

738

References

739

- Weston D, Stevens K. Interference of wide-band sound in shallow water. *J. Sound Vib.* 21(1):57–64. **1972**. 740
- Chuprov S. Interference structure of a sound field in a layered ocean. *Ocean Acoust., Curr. State.* 71–91. **1982**. 741
- Ianniello J. Recent developments in sonar signal processing. *IEEE Signal Proc. Magazine*, 15(4):27–40. **1998**. 742
- Thode AM. Source ranging with minimal environmental information using a virtual receiver and waveguide invariant theory. *J. Acoust. Soc. Am.*, 108(4):1582–1594. **2000**. 743
744
- Kuperman WA, D'Spain GL. Ocean acoustic interference phenomena and signal processing. *Ocean Acoust. Interfer. Phenom. Signal Proc.* 621 **2002**. 745
746
- Rouseff D, Spindel RC. Modeling the waveguide invariant as a distribution. *AIP Conf. Proc., Amer. Inst. Phys.* 621:137–150. **2002**. 747
748
- Baggeroer AB. Estimation of the distribution of the interference invariant with seismic streamers. *AIP Conf. Proc., Amer. Inst. Phys.* 621:151–170. **2002**. 749
750
- Yang T. Beam intensity striations and applications. *J. Acoust. Soc. Am.*, 113(3):1342–1352. **2003**. 751
- Heaney KD. Rapid geoacoustic characterization using a surface ship of opportunity. *IEEE J. Oceanic Engrg.*, 29(1):88–99. **2004**. 752
753
- Cockrell KL, Schmidt H. Robust passive range estimation using the waveguide invariant. *J. Acoust. Soc. Am.*, 127(5):2780–2789. **2010**. 754
755
- Rouseff D, Zurk LM. Striation-based beam forming for estimating the waveguide invariant with passive sonar. *J. Acoust. Soc. Am. Express Lett.*, 130:76–81. **2011**. 756
757
- Harrison CH. The relation between the waveguide invariant, multipath impulse response, and ray cycles. *J. Acoust. Soc. Am.*, 129(5):2863–2877. **2011**. 758
759
- Emmetiere R, Bonnel J, Gehant M, Cristol X, Chonavel Th. Understanding deep-water striation patterns and predicting the waveguide invariant as a distribution depending on range and depth. *J. Acoust. Soc. Am.*, 143(6):3444–3454. **2018**. 760
761
762
- Emmetiere R, Bonnel J, Cristol X, Gehant M, Chonavel T. Passive source depth discrimination in deep-water. *IEEE J. Select. Topics Signal Process.*, 13(1):185–197. **2019**. 763
764
- Kuznetsov GN, Kuzkin VM, Pereselkov SA. Spectrogram and localization of a sound source in a shallow sea. *Acoust. Phys.*, 63(4):449–461. **2017**. 765
766
- Pereselkov SA, Kuz'kin VM. Interferometric processing of hydroacoustic signals for the purpose of source localization. *J. Acoust. Soc. Am.* 151:666–676. **2022**. 767
768
- Ehrhardt M, Pereselkov SA, Kuz'kin VM, Kaznacheev I, Rybyanets P. Experimental observation and theoretical analysis of the low-frequency source interferogram and hologram in shallow water. *J. Sound Vibr.* 544:117388. **2023**. 769
770
771
- Pereselkov S, Kuz'kin V, Ehrhardt M, Tkachenko S, Rybyanets P, Ladykin N. Use of interference patterns to control sound field focusing in shallow water. *J. Mar. Sci. Eng.* 11:559. **2023**. 772
773
- Pereselkov S, Kuz'kin V, Ehrhardt M, Matvienko Y, Tkachenko S, Rybyanets P. The formation of 2D holograms of a noise source and bearing estimation by a vector scalar receiver in the high-frequency band. *J. Mar. Sci. Eng.* 12:704. **2024**. 774
775
776
- Kuz'kin VM, Pereselkov SA, Zvyagin VG, Malykhin AYu, Prosovetskiy DYU. Intense internal waves and their manifestation in interference patterns of received signals on oceanic shelf. *Phys. Wave Phenom.*, 26(2):160–167. **2018**. 777
778
779

21. Badiey M, Kuz'kin VM, Lyakhov GA, Pereselkov SA, Prosovetskiy DYU, Tkachenko SA. Intense internal waves and their manifestation in the interference patterns of received signals on oceanic shelf. Part II. *Phys. Wave Phenom.* 27:313–319. **2019.**
22. Badiey M and SWARM'95 group. Cruise Report. Ocean Acoustic Experiments in Support of Shallow Water Acoustic Remote Measurements (SWARM). *University of Delaware P.* 72. **1995.**
23. Apel JR, Badiey M, Chiu C-S, Finette S, Headrick RH, Kemp J, Lynch JF, Newhall AE, Orr MH, Pasewark BH, Tielburger D, Turgut A, von der Heydt K, Wolf SN. An overview of the SWARM 1995 shallow-water internal wave acoustic scattering experiment. *IEEE J. Ocean. Engrg.*, 22:465-500. **1997.**
24. Serebryany AN. Manifestation of the properties of solitons in internal waves on the shelf. *Izv. Acad. Sci. USSR, Phys. Atmosphere Ocean*, 29(2):285-293. **1993.**
25. Ostrovsky LA, Stepanyants YuA. Do internal solitons exist in the ocean? *Reviews of Geophysics* 27:293-310 **1989.**
26. Konyaev KV, Sabinin KD. Waves inside the ocean. *St. Petersburg, Gidromet. Publ.*, 271 p. **1992.**
27. Katsnelson BG, Pereselkov SA. Low-frequency horizontal acoustic refraction caused by internal wave solitons in a shallow sea. *Acoust. Phys.*, 46(6):684-691. **2000.**
28. Pereselkov S, Kuz'kin V, Ehrhardt M, Tkachenko S, Rybyanets, P, Ladykin, N. Three-Dimensional Modeling of Sound Field Holograms of a Moving Source in the Presence of Internal Waves Causing Horizontal Refraction. *J. Mar. Sci. Eng.* 11, 1922. **2023**
29. Pereselkov S, Kuz'kin V, Ehrhardt M, Tkachenko S, Pereselkov A, Ladykin N, Influence of Intense Internal-Waves Traveling Along an Acoustic Path on Source Holographic Reconstruction in Shallow Water. *J. Mar. Sci. Eng.* 13, 1409. **2025**
30. Harris PT, Baker EK (eds). Seafloor Geomorphology as Benthic Habitat: GeoHab Atlas of Seafloor Geomorphic Features and Benthic Habitats. *Elsevier*, 936 p. **2012.**
31. Micallef A, Krastel S, Savini A (eds). Submarine Geomorphology. *Springer*, 636 p. **2018.**
32. Chiocci FL, Ridente D. Seafloor Mapping along Continental Shelves: Research and Applications. *Springer*, 276 p. **2015.**
33. Lecours V, Dolan MFJ, Micallef A, Lucieer VL (eds). Marine Geomorphometry: Geomorphometry Concepts and Applications to Marine Environments. *MDPI Books*, 222 p. **2020.**
34. GEBCO Compilation Group. The GEBCO_2023 Grid — global bathymetric data set. *GEBCO. Available online:* https://www.gebco.net/data_and_products/gridded_bathymetry_data/ **2023.**
35. Ashley GM. Classification of large-scale subaqueous bedforms: a new look at an old problem. *Journal of Sedimentary Research*, 60(1):160–172. **1990.**
36. Kuperman WA, Ingenito F (eds). Acoustics of the Ocean Bottom. *Hemisphere Publishing Corporation, Washington, DC.* 454 p. **1980.**
37. Hamilton E (ed). Acoustics of Marine Sediments. *Springer US / Plenum Press, New York.* 498 p. **1970.**
38. Brekhovskikh LM, Lysanov YP. Fundamentals of Ocean Acoustics. *Springer.* **2013.**
39. Jensen FB, Kuperman WA, Porter MB, Schmidt H, Tolstoy A. Computational Ocean Acoustics. *Springer.* **2011.**
40. Lin Y-T, Porter MB, Sturm F, Isakson MJ, Chiu C-S. Introduction to the special issue on three-dimensional underwater acoustics. *J. Acoust. Soc. Am.*, 146(3):1855–1857. **2019.**
41. Liu W, Zhang L, Wang W, Wang Y, Ma S, Cheng X, Xiao W. A three-dimensional finite difference model for ocean acoustic propagation and benchmarking for topographic effects. *J. Acoust. Soc. Am.*, 150(2):1140–1156. **2021.**
42. Tu H, Wang Y, Liu W, Yang C, Qin J, Ma S, Wang X. Application of a Spectral Method to Simulate Quasi-Three-Dimensional Underwater Acoustic Fields. *J. Sound Vibr.*, 545:117421. **2023.**
43. Larsson E, Abrahamsson L. Helmholtz and parabolic equation solutions to a benchmark problem in ocean acoustics. *J. Acoust. Soc. Am.*, 113(5):2446–2454. **2003.**
44. Smith KB, Tappert FD. UMPE: The University of Miami Parabolic Equation Model. *Version 1.1 "MPL Technical Memorandum 432", P.* 96. **1993.**
45. Tappert FD. The parabolic approximation method. *Lecture Notes in Physics*, V. 70, Eds. J.B. Keller, J.S. Papadakis, Eds., *Wave Propagation and Underwater Acoustics, Springer-Verlag, New York, Chapter 5, pp.* 224-287. **1977.**
46. Lin Y-T. Three-dimensional boundary fitted parabolic-equation model of underwater sound propagation. *J. Acoust. Soc. Am.*, 146(3):2058–2067. **2019.**

47. Heaney KD, Campbell RL. Three-dimensional parabolic equation modeling of mesoscale eddy deflection. *J. Acoust. Soc. Am.*, 139(2):918–926. **2016**. 834
48. Ivansson S. Local accuracy of cross-term corrections of three-dimensional parabolic-equation models. *J. Acoust. Soc. Am.*, 146(3):2030–2040. **2019**. 835
49. Lee K, Seong W, Na Y. Three-dimensional Cartesian parabolic equation model with higher-order cross-terms using operator splitting, rational filtering, and split-step Padé algorithm. *J. Acoust. Soc. Am.*, 146(3):2030–2040. **2019**. 836
50. Lee K, Seong W, Na Y. Split-step Padé solver for three dimensional Cartesian acoustic parabolic equation in stair-step representation of ocean environment. *J. Acoust. Soc. Am.*, 146(3):2050–2057. **2019**. 837
51. Porter MB. Beam tracing for two- and three-dimensional problems in ocean acoustics. *J. Acoust. Soc. Amer.*, 146(3):2016–2029. **2019**. 838
52. Porter MB. Bellhop3d User Guide. La Jolla, CA: Heat, Light, and Sound Research, Inc. **2016**. 839
53. Collins MD. The adiabatic mode parabolic equation. *J. Acoust. Soc. Am.* 94:2269–2278. **1993**. 840
54. Trofimov MY, Kozitskiy S, Zakharenko A. A mode parabolic equation method in the case of the resonant mode interaction. *Wave Motion*, 58:42–52. **2015**. 841
55. Petrov PS, Sturm F. An explicit analytical solution for sound propagation in a three-dimensional penetrable wedge with small apex angle. *J. Acoust. Soc. Amer.*, 139(3):1343–1352. **2016**. 842
56. Kohler W, Papanicolaou GC Wave propagation in a randomly inhomogeneous ocean. In: Keller JB Papadakis JS (Eds.), *Wave Propagation and Underwater Acoustics Lecture Notes in Physics, Springer*, 70:153–223. **1977**. 843
57. Weinberg H, Burridge R. Horizontal ray-theory for ocean acoustics. *J. Acoust. Soc. Am.* 55:63–79. **1974**. 844
58. Jensen FB, Kuperman WA. Sound propagation in a wedge-shaped ocean with a penetrable bottom. *J. Acoust. Soc. Am.* 67:1564–1566. **1980**. 845
59. Buckingham M. Theory of three-dimensional acoustic propagation in a wedgelike ocean with a penetrable bottom. *J. Acoust. Soc. Am.* 82:198–210. **1987**. 846
60. Deane G, Buckingham M. An analysis of the three-dimensional sound field in a penetrable wedge with a stratified fluid or elastic basement. *J. Acoust. Soc. Am.* 93:1319–1328. **1993**. 847
61. Fawcett J. Modeling three-dimensional propagation in an oceanic wedge using parabolic equation methods. *J. Acoust. Soc. Am.* 93:2627–2632. **1993**. 848
62. Westwood E. Broadband modeling of the three-dimensional penetrable wedge. *J. Acoust. Soc. Am.* 92:2212–2222. **1992**. 849
63. Sturm F. Examination of signal dispersion in a 3-D wedge-shaped waveguide using 3DWAPE. *Acta Acust. united Ac.* 88:714–717. **2002**. 850
64. Sturm F, Fawcett J. Numerical simulation of the effects of the bathymetry on underwater sound propagation using three-dimensional parabolic equation models. *Technical Report SM-342, SACLANT Undersea Research Centre, La Spezia, Italy*. **1993**. 851
65. Sturm F, Kampanis N. Accurate treatment of a general sloping interface in a finite-element 3-D narrow-angle PE model. *J. Comput. Acoust.* 15:285–318. **2007**. 852
66. Sturm F. Numerical study of broadband sound pulse propagation in three-dimensional shallow water waveguides. *J. Acoust. Soc. Am.* 117:1058–1079. **2005**. 853
67. Ballard MS, Sagers JD. Measurements and modeling of acoustic propagation in a scale model canyon. *J. Acoust. Soc. Am.* 146:1858–1866. **2019**. 854
68. Barclay DL, Barclay DR, Lin YT. Three-dimensional ambient noise modeling in a submarine canyon. *J. Acoust. Soc. Am.* 146:1956–1967. **2019**. 855
69. DeCourcy BJ, Lin YT. Spatial and temporal variation of three-dimensional ship noise coherence in a submarine canyon. *J. Acoust. Soc. Am.* 153:1042–1051. **2023**. 856